DEPARTMENT OF PHYSICS AND ASTRONOMY
RUPRECHT-KARLS UNIVERSITY

MASTER THESIS

Noise reduction of local spin rotations and analysis of the three-component vector soliton formation

---

Submitted by
David Feiz Bakhsh Bazargani
born in Bad Dürkheim,
Germany

Supervisor:
Prof. Dr. Markus Oberthaler

This Master Thesis has been carried out by

David Feiz Bakhsh Bazargani

at the

Kirchhoff-Institut für Physik

January 29, 2024

"In all affairs it's a healthy thing now and then to hang a question mark on the things you have long taken for granted."

Bertrand Russell

Abstract

In order to detect quantum correlations between three-component vector solitons in a spin-1 Bose-Einstein condensate, the noise contribution of the local rotation setup has to be as low as possible. In our experimental setup, the positional fluctuations of the laser have been found to be the dominant source of noise. This thesis presents a scheme in which the laser, used for the generation of local rotations, is vertically pulsed 6 times, to effectively broaden the vertical intensity profile and achieve a homogeneous rotation amplitude. In compensating the relative motion between the condensate and laser, we observe a reduced fluctuation of the F_z amplitude. Locally rotating the state $m_F = 0$ leads to fluctuations of $\Delta^2 F_z = 0.21 \pm 0.02$. This deviates $15 - 30\%$ from the theoretically determined value $\Delta^2 F_z^{\mathrm{tri}} = 0.16$, but shows an improvement by an order of magnitude compared to the results obtained via a continuous sweep of the vertical laser position. Applying a $\pi/2$ rotation to the $m_F = -1$ state leads to a fluctuation of the rotation angle of $\sqrt{\Delta^2 \alpha} = (5.62 \pm 0.84)^\circ$, which is on the same order of magnitude as the extension of the coherent state, $\alpha_{\mathrm{coh}} \approx 6.2^\circ$. The enhanced precision of the local rotation setup is used to gain a better understanding of the soliton splitting process. First observations show that the lowest fluctuations of the combined variables $F_z^{\pm} = F_z^{\mathrm{left}} \pm F_z^{\mathrm{right}}$ fall slightly below the shot noise limit, which is represented by the ratio between the experimental and theoretical (coherent state) value, $r^+ = 0.81 \pm 0.11$ and $r^- = 0.86 \pm 0.13$. Even after separating the evaluation regions to account for classical correlations at the boundary, this result remains consistent up to a separation of 10.08 µm. The analysis of the atom number distribution between the different bright components of the soliton shows a deviation from the coherent state level $\sigma^2_{\mathrm{coh}} = 1$. The lowest value, obtained for the difference $N^- = N^{\mathrm{l}} - N^{\mathrm{r}}$ is $\Delta^2 N^- = 1.40 \pm 0.22$, after normalisation with the total atom number.

Zusammenfassung

Um Quantenkorrelationen zwischen dreikomponentigen Vektorsolitonen in Spin-1 Bose-Einstein Kondensaten nachweisen zu können, muss das Rauschen, welches durch den lokalen Rotationsaufbau erzeugt wird, so gering wie möglich sein. In unserem Versuchsaufbau sind die Positionsfluktuationen des Lasers als dominante Rauschquelle festgestellt worden. Diese Arbeit präsentiert ein Verfahren, bei dem der Laser, der für die Erzeugung lokaler Rotationen verwendet wird, 6 mal vertikal gepulst wird, um das vertikale Intensitätsprofil zu verbreitern und ein homogenes Rotationsprofil zu erreichen. Durch eine Kompensation der relativen Bewegung zwischen Kondensat und Laser ist eine Verringerung der Fluktuation der F_z Amplitude zu beobachten. Eine lokale Rotation des Zustands $m_F = 0$ führt zu Fluktuationen von $\Delta^2 F_z = 0.21 \pm 0.02$. Diese weicht $15 - 30\%$ vom theoretisch erwarteten Wert $\Delta^2 F_z^{\mathrm{tri}} = 0.16$ ab, zeigt aber eine Verbesserung um eine Größenordnung im Vergleich zu den Ergebnissen, welche für eine kontinuierliche Rampe der vertikalen Laserposition bestimmt wurden. Eine $\pi/2$-Rotation des Zustands $m_F = -1$ führt zu Fluktuationen des Rotationswinkels $\sqrt{\Delta^2 \alpha} = (5.62 \pm 0.84)^\circ$, was in der gleichen Größenordnung ist wie die Ausdehung des kohärenten Zustands, $\alpha_{\mathrm{coh}} \approx 6.2^\circ$. Die verbesserte Genauigkeit des lokalen Rotationsaufbaus wird verwendet, um ein besseres Verständnis des Separationsprozesses von Solitonen zu erlangen. Erste Beobachtungen zeigen, dass die kleinsten Fluktuationen der kombinierten Variablen $F_z^{\pm} = F_z^{\mathrm{left}} \pm F_z^{\mathrm{right}}$ leicht unterhalb des Schrotrauschlimits sind, was durch das Verhältnis zwischen dem experimentellen und theoretischen (kohärenter Zustand) Wert $r^+ = 0.81 \pm 0.11$ und $r^- = 0.86 \pm 0.13$ dargestellt wird. Auch nach Separation der Auswertungsbereiche, um klassische Korrelationen an der Grenze zu berücksichtigen, bleiben die Ergebnisse bis zu einer Separation von 10.08 µm konsistent. Die Analyse der Atomzahlverteilung zwischen den unterschiedlichen hellen Komponenten der Solitonen zeigen eine Abweichung vom erwarteten Level eines kohärenten Zustands, $\sigma^2_{\mathrm{coh}} = 1$. Der niedrigste Wert wurde für die Differenz $N^- = N^{\mathrm{l}} - N^{\mathrm{r}}$ bestimmt und ist $\Delta^2 N^- = 1.40 \pm 0.22$, nachdem mit der Gesamtatomzahl normiert wurde.

Contents

Chapter 1.

Introduction

Modern approaches in the experimental study of quantum mechanical phenomena are often concerned with ultra cold quantum gases, where atom clouds are kinetically frozen to very low temperatures and which provide a high level of experimental control. A particular milestone was the generation of the so-called Bose-Einstein-condensate, an exotic state of matter, where a major fraction of the atoms occupy one quantum state. As a result, the condensate can be described by one single wavefunction and is said to manifest quantum mechanics on macroscopic scales.

First proposed by S. Bose [1] and later theoretically predicted for matter by A. Einstein in 1924 [2], it was until 1995 that the first BECs were realised experimentally by C. Wieman and E. Cornell at the JILA [3] using rubidium (^{87}Rb) and by W. Ketterle's group at the MIT [4], who condensed sodium atoms (^{23}Na), resulting in the shared win of the Nobel prize. Main candidates for the realisation of BECs have been alkali metals, e.g. ^{7}Li [5], ^{41}K [6], and alkaline earth metals, e.g. ^{40}Ca [7], ^{84}Sr [8], providing one and two valence electrons and appearing to be particularly suitable for the application of the common cooling and trapping techniques. But also lanthanide atom BECs using e.g. ^{164}Dy [9] or ^{170}Yb [10] were accomplished, mixture experiments comprising two atomic species developed [11] and molecules condensed to a BEC [12]. Recently, even a BEC orbiting the earth, as a part of an international research laboratory, has been built [13].

The here presented work will be concerned with a spin-1 BEC in the quasi one-dimensional regime consisting of ^{87}Rb atoms. This type of condensate is also called a *spinor*-BEC [14], because it provides the spin as a degree of freedom, suitable for the investigation of the interplay between spatial and spin dynamics.
In the theoretical mean-field limit of spin-1 BECs solitons, but in particular three-component vector solitons were predicted as analytical solutions of the Manakov model [15]. At their heart, solitons, short for solitary waves, are non-dispersive wave packets propagating at a constant velocity, while maintaining their structure. In order to support stable solutions, the system has to provide a non-linearity to counteract the dispersive effects.
In recent years this experimental platform has been used to successfully generate vector solitons in our group ([16], [17]). To this end, a laser setup is employed to induce spatially localised radio-frequency transitions, further referred to as local rotations in this thesis. The subsequent characterisation of the macroscopic properties of the solitons showed a good agreement with the underlying theoretical model. The richness of these vector solitons compared to e.g. simple dark solitons arises from the fact that not only studies of the macroscopic properties can be conducted, but also of the internal structure, namely the spin. Future prospects are geared towards the exploration of quantum correlations in scenarios like soliton collisions [17]. Detecting quantum correlations is in general experimentally challenging, because they are usually overshadowed by different kinds of classical correlations caused by the

experimental setup, but is at the heart of revealing entanglement between systems. In this thesis, an experimental setup will be presented which aims to reduce the technical noise in the preparation of three-component vector solitons, to be able to detect signals below the shot noise limit in future experiments. To this end, the vertical positional fluctuation between the condensate and laser, necessary to generate the soliton, will be eliminated utilising a pulse sequence in vertical direction in order to provide a vertically broader and homogeneous intensity profile.
Additionally, the soliton formation phase will be of interest, where two solitons emerge out of an initial local density perturbation. Thereupon, we want to quantify if we can prepare solitons on coherent state level. We use observables like the atom number and spin to compare the fluctuations of combined variables as sums and differences between the two solitons (EPR-variables) to the shot-noise limit set by a coherent state.

Chapter 2.

Theoretical Background

The aim of this chapter is to build the basic understanding of spinor bose gases, in particular of the spin-1 Bose Einstein condensates. We will first start with the general symmetry assumptions and the operators that can be concluded from these. Further, the basic concepts of a spin-1 BEC and the theory behind solitons will be introduced.

2.1 The Spin-1/2 system

Many physical problems in atomic physics can be reduced to a so-called pseudo spin-1/2 system, since the coupling and transition of states can be mapped onto the two level systems. Revisiting the ideas of the spin-1/2 system is therefore an instructive way to introduce the concept of spin observables and understand the necessity of the unitary transformations. We can then use these ideas then to build the framework of the spin-1 system in a similar way. More details can be found in [18], [19] and [20].

The spin-1/2 system is considered the most fundamental spin system because it can be represented by the generic quantum mechanical two-level system. The basis states in the single particle description can be written as

$$|0\rangle = \begin{pmatrix} 1 \\ 0 \end{pmatrix} \quad \text{and} \quad |1\rangle = \begin{pmatrix} 0 \\ 1 \end{pmatrix} \tag{2.1}$$

and the wave function of a pure state can be described by the coherent superposition

$$|\psi\rangle = e^{i\phi_L} \cos(\frac{\theta}{2})|0\rangle + e^{-i\phi_L} \sin(\frac{\theta}{2})|1\rangle. \tag{2.2}$$

The Larmor phase ϕ_L is defined as the phase difference between the states $|0\rangle$ and $|1\rangle$, so $\phi_L = \phi_0 - \phi_1$. The two angles $\phi_L \in [0, 2\pi]$ and $\theta \in [0, \pi]$ define the resulting state uniquely and its norm must be $\langle\psi|\psi\rangle = 1$. It can most conveniently be represented on the surface of the so-called Bloch sphere (see fig. 2.1), which also serves as a good tool to visualise the transformation of the states. Since the system contains only two free parameters, the transformations are group elements of SU(2), which contains the complex 2x2 matrices with unit determinant. If the quantisation axis is given along the z-axis, we can parametrise the transformations by defining the Pauli matrices first,

$$S_x = \frac{1}{2}\begin{pmatrix} 0 & 1 \\ 1 & 0 \end{pmatrix}, \quad S_y = \frac{1}{2}\begin{pmatrix} 0 & -i \\ i & 0 \end{pmatrix}, \quad S_z = \frac{1}{2}\begin{pmatrix} 1 & 0 \\ 0 & -1 \end{pmatrix}. \tag{2.3}$$

They fulfil the necessary commutation relations $[S_i, S_j] = i\epsilon_{ijk}S_k$ for $i, j, k \in \{x, y, z\}$ and ϵ_{ijk} being the Levi-Civita symbol. Including $\mathbb{1}_{2x2}$ we have the complete set of

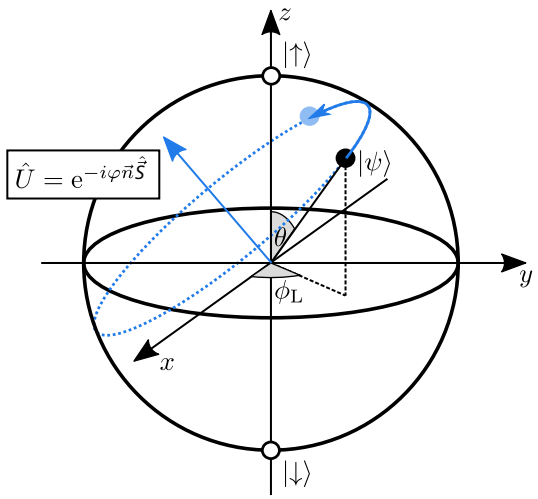

FIGURE 2.1: Representation of a state $|\psi\rangle$ on the Bloch sphere including the unitary matrix U for the rotation. Figure adapted from [21].

operators which form the basis for all hermitian operators acting on the spin-1/2 Hilbert space $\mathbb{C}^2$.
The spin operators 2.3 are generators of the rotations on the Bloch-sphere. If we want to consider the rotation by a finite angle φ, we can use these generators to define the unitary transformation

$$U(n,\varphi) = e^{-i\varphi \mathbf{nS}}, \tag{2.4}$$

where **n** denotes the rotation axis. For rotations around the z-axis this can be simply written as

$$U_z(\varphi) = e^{-i\varphi S_z}, \tag{2.5}$$

Applying the rotation matrix on the ket-vector $|\psi\rangle$ allows us to calculate its rotation on the sphere as

$$|\psi\rangle_R = U_z|\psi\rangle. \tag{2.6}$$

This process would be equivalent to the Schrödinger picture where a quantum state is considered to evolve in time. But one could also just rotate the system and keep the state "unchanged", in analogy to the Heisenberg picture. The rotation matrices transform according to

$$e^{i\varphi S_j} S_i e^{-i\varphi S_j} = S_i cos(\varphi) + \epsilon_{ijk} S_k sin(\varphi), \tag{2.7}$$

as been calculated in literature before [18] with $\hbar = 1$. From this result we can conclude that the axis of our systems can be conveniently rotated and ultimately mapped onto the other axes. It is worth to note that by applying eq. 2.6 we can easily describe the dynamics of our state, while eq. 2.7 gives us a tool for the implementation of the necessary readout schemes discussed later in section 3.2.5.

2.2 Spin-1

In comparison to the spin-1/2 case, the spin-1 system of our experiment contains three magnetic components $m_F \in \{-1, 0, +1\}$. The quantum state in the single-particle representation can be written as

$$|\psi\rangle = c_1 e^{i\phi_L/2}|1\rangle + c_0 e^{i\phi_S}|0\rangle + c_{-1} e^{-i\phi_L/2}|-1\rangle, \tag{2.8}$$

where the real coefficients satisfy again the normalisation $\sum_i |c_i|^2 = 1$. The Larmor phase denotes the phase difference between the side modes $|\pm 1\rangle$ as $\phi_L = \phi_{+1} - \phi_{-1}$ and the spinor phase the difference between $|0\rangle$ and $|\pm 1\rangle$, $\phi_S = \phi_0 - (\phi_{+1} + \phi_{-1})/2$. The additional free parameters give rise to an extended set of rotation operators, which are defined by the Lie group SU(3). We can define 8 operators (generators) that once again serve as a basis for all hermitian operators necessary to act on the spin-1 Hilbert space. Analogously to the spin-1/2 case discussed before, we can first define the three spin operators

$$f_x = \frac{1}{\sqrt{2}}\begin{pmatrix} 0 & 1 & 0 \\ 1 & 0 & 1 \\ 0 & 1 & 0 \end{pmatrix}, \quad f_y = \frac{1}{\sqrt{2}}\begin{pmatrix} 0 & -i & 0 \\ i & 0 & -i \\ 0 & i & 0 \end{pmatrix}, \quad f_z = \begin{pmatrix} 1 & 0 & 0 \\ 0 & 0 & 0 \\ 0 & 0 & -1 \end{pmatrix}, \tag{2.9}$$

which fulfil the commutation relation $[f_i, f_j] = i\epsilon_{ijk} f_k$. For later use (see sec. 2.3.2) we introduce the vector of spin-1 matrices $\mathbf{f} = (f_x, f_y, f_z)^T$. To define a spin-1 state unambiguously the three spin operators do not suffice but additional quadrupole operators have to be defined to achieve a complete set of eight operators as a full representation of SU(3), defining all possible rotations of the system. For this thesis only the three spin operators will be considered, since for the analysis of solitons only the SU(2)-subspace is relevant. The state can be represented on a sphere again. In contrast to spin-1/2, the state does not just exist on the surface of the spin sphere but can also be inside of it.

2.3 A brief theory of Bose Einstein condensates

This section introduces the basic ideas and concepts necessary to describe spin-1 Bose-Einstein condensates. At first the Hamiltonian will be presented, followed by the Thomas-Fermi approximation and the mean-field picture of this system. In depth derivations and further information are given in [22], [23], [14] and [24].

2.3.1 The Gross Pitaevskii equation - a mean field model

In order to describe a quantum many-body system, quantum fields $\Psi(\mathbf{r}, t)$ are usually chosen as the foundation. The appropriate Hamiltonian to describe an interacting Bose gas in second quantisation is written as

$$\begin{aligned} H = &\int \mathrm{d}\mathbf{r}\Psi^\dagger(\mathbf{r}, t)(-\frac{\hbar^2}{2m}\nabla^2 + V_{\text{ext}}(\mathbf{r}, t))\Psi(\mathbf{r}, t) \\ &+ \frac{1}{2}\int \mathrm{d}\mathbf{r}\mathrm{d}\mathbf{r}'\Psi^\dagger(\mathbf{r}, t)\Psi^\dagger(\mathbf{r}', t)U(\mathbf{r}, \mathbf{r}')\Psi(\mathbf{r}', t)\Psi(\mathbf{r}, t), \end{aligned} \tag{2.10}$$

where V_{ext} denotes an external potential and $U(\mathbf{r}, \mathbf{r}')$ the interaction potential. From the Heisenberg equation $i\hbar\partial_t\Psi(\mathbf{r}, t) = -[H, \Psi(\mathbf{r}, t)]$ and using the bosonic commutation relations $[\Psi(\mathbf{r}, t), \Psi^\dagger(\mathbf{r}', t)] = \delta(\mathrm{r} - \mathrm{r}')$ one can conclude the time evolution of the quantum field operator.

In 1961, Lev P. Pitaevskii [25] and Eugene P. Gross [26] independently used the ansatz to expand these quantum fields in terms of their expectation value and quantum fluctuation term

$$\Psi(\mathbf{r}, t) = \langle\Psi(\mathbf{r}, t)\rangle + \delta\Psi(\mathbf{r}, t). \tag{2.11}$$

They were interested in the basic properties of Bose Einstein condensates, so assumed that the system is at zero temperature. Doing so allows to neglect the then

thermal fluctuations, $\delta\Psi(\mathbf{r},t) = 0$. In that manner, the field operator can be replaced by its expectation value, which itself is just a complex function, often referred to as *order parameter* of the mean field phase, according to $\langle\Psi(\mathbf{r},t)\rangle = \psi(\mathbf{r},t)$.

The second necessary assumption concerns the interaction of the particles inside the BEC. For systems at very low temperatures the relevant atomic interaction is the *s-wave* scattering, which is characterised by the scattering length a through the interaction constant $g = \frac{4\pi\hbar^2}{m}a$, where m is the atomic mass. For that to hold, the gas is assumed to be dilute, i.e. the condition $\bar{n}a^3 \ll 1$ fulfilled, with $\bar{n}$ being the average density, meaning that the inter-particle distance is much larger than the scattering length. Hence, the interaction is mediated by a delta-like potential $U(\mathbf{r},\mathbf{r}') = g\delta(\mathbf{r}-\mathbf{r}')$. The sign of the scattering length determines whether the interaction is attractive ($a < 0$) or repulsive ($a > 0$). For ^{87}Rb the interaction is repulsive.

The concepts presented before correspond also to the limit of large populations, hence high densities, and weak interactions, where quantum fluctuations become negligible compared to classical statistical fluctuations. This picture is called *mean-field theory* and can be applied to successfully describe an ultra-cold many-body quantum system. Altogether the Gross-Pitaevskii equation is formulated as

$$i\hbar\partial_t\psi(\mathbf{r},t) = (-\frac{\hbar^2}{2m}\nabla^2 + V_{\text{ext}} + g|\psi(\mathbf{r},t)|^2)\psi(\mathbf{r},t). \tag{2.12}$$

One should note that the fields $\psi(\mathbf{r},t)$ introduced above determine the particle number density of the system $|\psi(\mathbf{r},t)|^2 = n(\mathbf{r},t)$ and fix the total particle number according to $\int d\mathbf{r}n(\mathbf{r},t) = N$. For time-independent potentials the energy is conserved and the wavefunction can be decomposed into $\psi(\mathbf{r},t) = \psi(\mathbf{r})e^{-i\frac{\mu t}{\hbar}}$. This separates the time-evolution and yields the stationary GPE. We further introduced the chemical potential $\mu = \partial E/\partial N$, originating from the systems statistical nature of a grand-canonical ensemble. However, eq. 2.12 has the form of a non-linear Schrödinger equation and reduces in the absence of interactions ($g = 0$, mean-field term vanishes) to the classical Schrödinger equation.

2.3.2 Spin-1 BEC and atomic interactions

Having discussed the general model of a Bose-Einstein condensate and assumptions appropriate to describe these systems, we can modify the model according to the specific needs of our experiment. An extensive derivation from first principles of the following concepts can be found in [24]. As will be seen in sec. 3.2.1, the ground-state of our experimental system are the hyperfine levels $F = 1$ and $F = 2$ which possess $m_F = 2F + 1$ magnetic states $|F, m_F\rangle$. This magnetic hyperfine sublevels separate in an external magnetic field, in our case an offset field, and shift the energy of each particle in the system but are also the cause of further interaction channels. The complete mean-field Hamiltonian comprises both terms, the non-interacting term and the interaction term according to $\mathcal{H} = \mathcal{H}_0 + \mathcal{H}_{\text{int}}$. The non-interaction Hamiltonian reads

$$\mathcal{H}_0 = \int \mathrm{d}^3x\psi^\dagger(-\frac{\hbar^2}{2m}\nabla^2 + V_{\text{ext}} + pf_z + qf_z^2)\psi, \tag{2.13}$$

with the mean-field order parameter ψ, which can be understood as the three component bosonic spinor field $\psi = (\psi_{+1}, \psi_0, \psi_{-1})^T$. The linear ($p$) and quadratic term ($q$) originate respectively from the linear and quadratic Zeeman effect. The linear

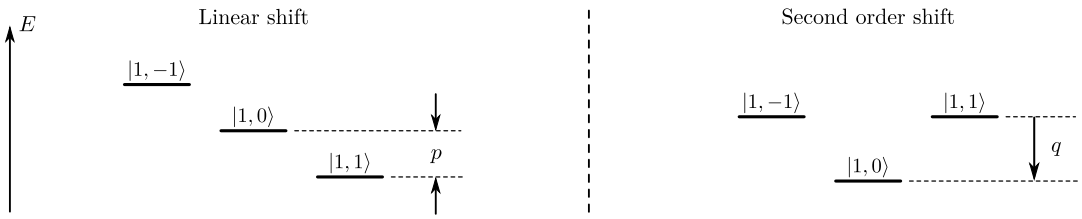

FIGURE 2.2: Linear and quadratic Zeeman shift due to an external magnetic field. Figure adapted from [16].

Zeeman effect shifts the magnetically sensitive state $|1, \pm 1\rangle$ in opposite directions (see fig. 2.2) and results in a Larmor precession of these states around the magnetic field. Setting this value to zero corresponds to a transformation to the rotating frame, which holds is also true when considering the atomic interactions discussed below. The contribution of interest for the dynamic of our system lies mainly in the second-order Zeeman shift. In contrast to p, the quadratic term results in a shift of the $|1, \pm 1\rangle$ states in the same direction, relative to $|1, 0\rangle$ (see fig. 2.2) . The interaction part of our Hamiltonian comprises the atomic interaction mediated by the density of the condensate, but due to the spin-degree of freedom also an spin-interaction term. The interaction term can be formulated as

$$\mathcal{H}_{\text{int}} = \int \mathrm{d}^3x \left(\frac{c_0}{2} n^2 + \frac{c_1}{2} \mathbf{F}^2\right), \tag{2.14}$$

where $n = |\psi|^2 = \psi^\dagger \psi$ denotes again the atom number density and $\mathbf{F} = \psi^\dagger \mathbf{f} \psi$ the spin density vector defined by the spin-1 matrices introduced in 2.2. The coefficients in 2.14 describe density-density interactions (c_0) and spin-spin interactions (c_1), defined as

$$c_0 = \frac{g_0 + 2g_2}{3} \quad \text{and} \quad c_1 = \frac{g_2 - g_0}{3}, \tag{2.15}$$

where we once again meet the interaction constant $g_\mathcal{F}$, just this time specifically denoting the two-body potential $V_\mathcal{F}(\mathbf{x}, \mathbf{y}) = g_\mathcal{F} \delta(\mathbf{x} - \mathbf{y})$ of total spin-$\mathcal{F}$ channel. Using the commutation relations for bosonic field operators in the second quantisation formalism one finds that only even total spins can contribute. As mentioned before only repulsive density-density interactions ($c_0 > 0$) are of interest in our experiment and as for ^{87}Rb-BECs the spin interactions are ferromagnetic ($c_1 < 0$). The interactions for which $c_1 > 0$ holds thus exert anti-ferromagnetic behaviour. Furthermore, for ^{87}Rb, the density interactions surpass the spin interactions largely $|c_1| \ll c_0$ and the ratio between the constants is $c_1/c_0 = 4.6 \times 10^{-3}$.

However, the interplay between the quadratic Zeeman shift q and the spin interaction term $\mathbf{F}^2$ can induce spin dynamical processes, namely spin-changing collision (SCC) which, if chosen appropriately dominate the overall dynamics. For their description it is usefull to consider quantum fields for a full quantum mechanical description, i.e. $\psi_j^{(\dagger)}(x) = \sum_k a_{j,k}^{(\dagger)} \xi_{j,k}(x)$, with the bosonic annihilation (creation) operator $a_{j,k}^{(\dagger)}$ and the spatial mode $\xi_{j,k}(x)$. Expanding now the spin-interaction in terms of these fields yields a term of the form $\psi_{+1}^\dagger \psi_{-1}^\dagger \psi_0 \psi_0 + h.c.$. If the atoms are initially prepared in $m_F = 0$, this term symmetrically redistributes them into the side-modes $m_F = \pm 1$. This process is controlled by the quadratic Zeeman term which can be used to bring the side-modes in resonance with $m_F = 0$ by an off-resonant microwave dressing of the system [27]. Consequentially, choosing high values of q,

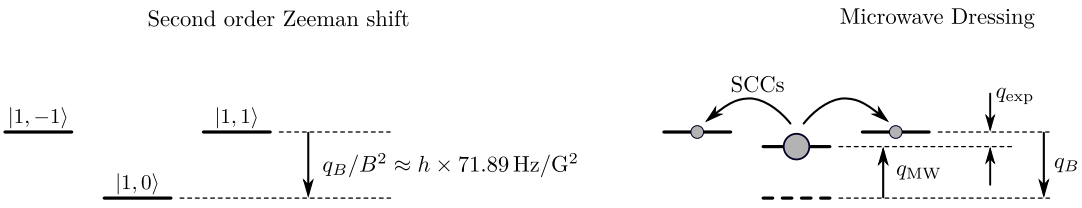

FIGURE 2.3: By controlling the q parameter of the second order Zeeman shift, we can bring the three hyperfine levels in resonance and induce spin-changing collision. Spin interactions cause a symmetric redistribution of the atoms from $|1,0\rangle$ to the side-modes and back. Tuning q far off-resonant suppresses this spin interactions. Figure adapted from [16]

i.e. no dressing of the system, suppresses this internal spin dynamics and allows to consider density-density interactions as the dominant process.

2.3.3 Thomas-Fermi approximation

In an experimental system with a sufficiently high atom number ($10^4 - 10^6$) the interaction energy dominates the kinetic energy, which can therefore be neglected in eq. 2.12. The density profile of the gas then takes the form

$$n(\mathbf{r}) = \frac{\mu - V_{\mathrm{ext}}(\mathbf{r})}{g} \tag{2.16}$$

Many experimental setups provide approximately harmonic potentials. In the simplistic 1D case they yield $V_{\mathrm{ext}} = \frac{m\omega^2 x^2}{2}$, with oscillator frequency ω and position x. From that the Thomas-Fermi radius of the condensate, i.e. the radius at which $n(r = R_{\mathrm{TF}}) = 0$, can be calculated to be

$$R_{\mathrm{TF}} = \frac{1}{\omega}\sqrt{\frac{\mu}{2m}}. \tag{2.17}$$

Plugging in the chemical potential in terms of the Thomas-Fermi radius in eq. 2.16 yields the inverted parabolic form of the condensate density, with its peak at the point where $V_{\mathrm{ext}} = 0$.
It is also instructive to consider a cylindrical symmetric harmonic potential, confining the atoms also in radial direction [28], resembling the situation our dipole lasers provide in the last step of our BEC generation (see sec. 3.1.2). The potential can be written as

$$V(\mathbf{x}) = \frac{m\omega_\perp^2}{2}(x^2 + y^2), \tag{2.18}$$

with trapping frequency $\omega_\perp = \omega_x = \omega_y$ (trapping forces act along xy-plane). Assuming that the energy corresponding to this frequency exceeds all relevant energy scales of the atomic gas, i.e. the interactions as

$$nc_0, nc_1 \ll \hbar\omega_\perp, \tag{2.19}$$

we can consider the transversal motion to be frozen and the system to be kinetically quasi-1D. The characteristic length scale is the *harmonic oscillator length*

$$a_\perp = \sqrt{\frac{\hbar}{m\omega_\perp}} \tag{2.20}$$

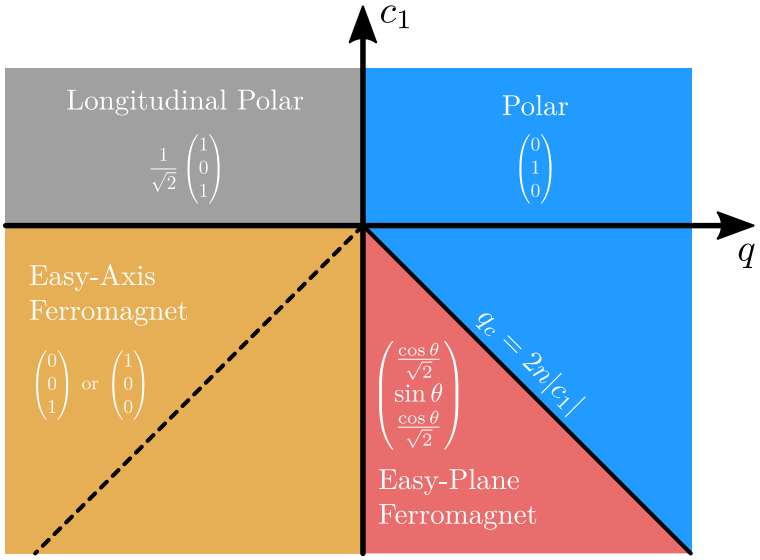

FIGURE 2.4: Mean-field phase diagram capturing the four different ground states of a spin-1 system defined by the spin interaction parameter c_1 and the quadratic Zeeman shift q. Figure adapted from [16]

In this scenario, a 1D version of the GPE can be considered while an effective interaction constant contains the information about the scattering events of the atoms in 1 dimensions [29],

$$g_{1D} = \frac{g}{2\pi a_\perp^2} = \frac{2\hbar^2}{m a_\perp} \tag{2.21}$$

2.3.4 Mean-field phase diagram

In order to understand the dynamics of our spin-1 BEC we have to initially characterise the groundstate of our system. The parameter of interest, controlling our system, is the second order Zeeman shift q. Due to the spin degrees of freedom in our system, it is possible to define different phases in the parameter space (q, c_1). Only the results and an intuitive picture are presented, in-depth derivations can be found in [14] and [24]. As discussed in the previous section we can divide the space spanned by q an c_1 at first by the latter parameter defining the type of spin-interactions inside the atomic species into an ferromagnetic ($c_1 < 0$) and anti ferromagnetic ($c_1 > 0$) phase. Further we notice that the energy functional we aim to minimise includes the spin-interaction term of eq. 2.14 and the magnetic shifts in eq. 2.13. Since we are interested in an expression of the form $\langle\psi|\mathcal{H}|\psi\rangle$, we can replace the spin-operators by their expectation values. The expression for the energy functional then yields

$$E = q\langle f_z\rangle^2 + \frac{c_1}{2}\langle \mathbf{F}\rangle^2, \tag{2.22}$$

where the linear magnetic shift has been dropped by a transformation into the rotating frame of the system. The spin interaction term has a rotational symmetry which is broken by the linear and quadratic Zeeman effect. For the anti-ferromagnetic case $c_1 > 0$ the system tries to minimise the spin per particle, thus the favourable spin expectation value is $\langle \mathbf{F}\rangle = 0$. For $q > 0$, the side-modes $|1, \pm 1\rangle$ get shifted "up", hence the population of the $|1, 0\rangle$-level becomes favourable for the system. This phase is called *polar state*. For $q < 0$ the side-modes are shifted energetically below the $|1, 0\rangle$-level and hence define the favourable energetic state, with an equal distribution over

both levels, called *longitudinal-polar state*. In the ferromagnetic case $c_1 < 0$ the system tries to maximise the spin per particle. Using the regime $q < 0$ we obtain two possible fully polarised spin states, the *easy-axis ferromagnet*. The side-modes are again the favourable choice of the system, but now the spin must be maximised, hence suppresses the simultaneous population of both levels. For $q < q_0 = -2n|c_1|$ a further magnetised state can be identified in the transverse plane, the *easy-plane ferromagnet*, where the spin-interaction term is competing with the quadratic Zeeman shift. The groundstate is an elongated spin in the transverse plane of the spin-sphere. Choosing $q = -2n|c_1|$ enables the production of spin-changing collisions discussed in 2.3.2. Intuitively, coming from the polar phase two atoms need to have the energy $n|c_1|$ to be symmetrically transferred to the side modes. A diagrammatic representation of the different phases can be found in fig. 2.4.

2.4 Manakov Model of Solitons

This section discusses the basics on solitons in a BEC. Once again a general discussion will be followed by the results necessary to understand the structure and properties of these objects. All calculations are done in a mean field theory, as this is sufficient to understand the properties of vector solitons to a good approximation. An extensive theoretical description can be found in [15]. Further, [30] and [31] provide additional insights on the underlying models and derivations of the results presented below.

The idea to study solitons is not new, since they have been first observed and studied in 1834 by John Scott Russel as non-dispersive waves travelling over long distances in water [32]. At this time, Russel called these peculiar objects "wave of translation", later named "solitary wave". The key properties of soltions is a constant velocity with which they propagate and a stable shape or structure, hence being non-dispersive wave packets. Later, theoretical calculations described a soliton as the solution of non-linear differential equations, which allowed them to be interpreted as an emerging feature in a non-linear dispersive medium, where the non-linearity compensates the dispersive effects. It appears hence clear that a great interest was found in non-linear optics, where the systems provide the necessary frame to study solitons. Also in communication [33], medicine [34] and biology [35] studies have been conducted and applications found. But it was not only the wave character that arised attention. The fact that solitons are not subject to superposition and collide elastically, maintaining their shape and velocity, called for a particle-like description, resulting in the now commonly used name *soliton*.

Moving to our system, in which we deal with a spinor BEC, we are particularly interested in the description of vector solitons, consisting of three distinct components. In order to find a proper description, we must include the kinetic as well as the interaction properties of the atoms, while ensuring that our system provides the necessary non-linearity. The appropriate Hamiltonian for this has been presented in sec. 2.3.2. In absence of an external potential ($V_{\text{ext}} = 0$) and the magnetic field shifts ($p = q = 0$) and for $c_1 = 0$ the system reduces to the so-called Manakov model [30]. The time-evolution is then equivalent to 2.12, without the potential term, resulting in the non-linear Schrödinger equation (NLSE)

$$i\hbar\partial_t\psi(\mathbf{r},t) = (-\frac{\hbar}{2m}\nabla^2 + \frac{c_0}{2}|\psi(\mathbf{r},t)|^2)\psi(\mathbf{r},t). \tag{2.23}$$

The non-linearity is provided by the density-density interaction, mediated by the interaction constant c_0, and the wave-function is generally interpreted as the spinor field introduced in 2.3.2 as $\psi = (\psi_{+1}, \psi_0, \psi_{-1})^T$ in the mean-field sense. Experimentally, this is achieved by choosing a large quadratic Zeeman shift q, to be deep in the polar phase. This effectively suppresses any internal spin dynamics, i.e. spin changing collision, by making this effect off-resonant. Then, we can neglect the spin interactions, if we consider that c_1 is much smaller than c_0, as explained in sec 2.3.2. In that fashion the only relevant interaction process are density interactions.

Vector soliton solutions were derived using e.g. inverse scattering theory (IST) ([36],[37]). The solitons we are interested in include so-called dark and bright solitons, which can be found in systems with repulsive inter-atomic interaction $c_0 > 0$. Originating from optics the terminology can also be understood in the BEC framework as local density depletions (dark) and density peaks (bright) in the condensate. We will consider only the 1D case in which the condensate is transversely tightly confined by a sufficiently high trapping frequency $\omega_\perp$ as discussed in sec. 2.3.3. This ensures that only the lowest oscillator mode is occupied in transversal direction. The solutions for the vector soliton components presented here are adapted from [16] and read

$$\psi_{\pm1}(x) = \sqrt{n_0} c_{\pm1} \eta \sin(\alpha) \operatorname{sech}[\kappa(x - x_0)] e^{i\varphi_{\text{kin}}} \quad \text{and} \tag{2.24}$$

$$\psi_0(x) = \sqrt{n_0}(i\cos(\alpha) + \sin(\alpha)\tanh[\kappa(x - x_0)]) e^{i\varphi_s}. \tag{2.25}$$

The soliton components are distributed over the different magnetic substates m_F of the $F = 1$ manifold, where the bright components sit in the side modes $|1, \pm1\rangle$ and the dark component in $|1, 0\rangle$. Together, they form a so-called bright-dark-bright soliton (BDB). κ is the inverse soliton width and is also included, together with the velocity v and chemical potential μ inside the parameter $\eta = \sqrt{1 - (\hbar^2\kappa^2 + v^2)/(m\mu)}$. The chemical potential can be introduced by subtracting it from eq. 2.23, effectively subtracting the phase evolution of the condensate caused by it. The position of the soliton is characterised by x_0. Furthermore, α is linked to $\tan(\alpha) = \hbar\kappa/mv$ and $c_{\pm1}$ are complex amplitudes, satisfying $|c_1|^2 + |c_{-1}|^2 = 1$, carrying the information about the distribution of the atoms among the bright components. It can be understood as the spin polarisation of the soliton system which is represented by the spin polarisation vector $\mathbf{c} = (c_1, c_{-1})^T$. As before, φ_s denotes the relative phase between the 0 and ±1 component, equivalent to the spinor phase. The new phase appearing here, φ_{kin}, is the kinetic phase of the bright components and is defined as

$$\varphi_{\text{kin}} = \frac{mv}{\hbar}(x - x_0) - \frac{1}{\hbar}\left(\frac{mv^2}{2} - \frac{\hbar^2\kappa^2}{2m}\right)t. \tag{2.26}$$

From the wavefunctions, the atom number densities in the different levels as well as the density of the entire system can be calculated by

$$n_{\pm1} = |\psi_{\pm1}(x)|^2 \tag{2.27}$$

$$n_0 = |\psi_0(x)|^2 \tag{2.28}$$

$$n = \sum_{m=0,\pm1} |\psi_m(x)|^2 \tag{2.29}$$

The condition ensuring the existence of these 3-component solitons, called non-singularity condition, gives a bound to the velocity and width by the chemical potential of the background density and is formulated as

$$\frac{\hbar^2\kappa^2}{m} + mv^2 \leq \mu. \tag{2.30}$$

This is equivalent to the parametrisation of a circle where the radius is given by the chemical potential. Equality of this equation is equivalent to only a single component dark soliton, inequality gives rise to the multi-component solutions. However, eq. 2.30 poses a condition on the possible properties of a soliton. For a fixed chemical potential, increasing the width of a soliton corresponds to a reduction of the velocity and vice versa.

The soliton density width can be calculated via the FWHM of the sech-function defining the bright component (eq. 2.24) to be

$$\text{FWHM} = \frac{2ln(1+\sqrt{2})}{\kappa}. \tag{2.31}$$

In contrast to single component solitons, the additional spin degree of freedom three component solitons inherit make them suitable to not just study their macroscopic properties, but also use them as a platform for spin physics. As presented in [17], preparing two solitons with a specific Larmor phase and letting them collide leads to different polarisations, depending on the initial phase difference. Since their in-depth study begun in recent years, it is a currently progressing field where the revelation of new features can fuel future research.

Chapter 3.

Experimental Setup

After laying the theoretical groundwork, we will now discuss the experimental basics of the spinor BEC experiment which is used as a platform for the generation of vector solitons. The following chapter will describe the experimental cycle we employ to cool our Rubidium atoms starting at room temperature to achieve the quasi one-dimensional spinor BEC and introduce some general tools necessary to manipulate the condensate to our needs.

Experimental Cycle
A usual experimental cycle includes three steps. First the BEC is generated, then we let the system evolve in time in order to allow for dynamical processes, followed by the readout. Each experimental cycle is fixed at 37s.

The road to a BEC follows in the main stages the standard sequence, which has been described in our system in various previous works (e.g. [21], [38]) and combines different cooling and trapping techniques necessary to overcome the temperature limits of the preceding steps in an ultra-high vacuum chamber. The atoms get transversely confined in a 2d-magneto optical trap (2d-MOT) from where they are loaded into a 3d-MOT after passing through a differential pumping stage connecting the 2d-MOT chamber with the ultra-high vacuum chamber. The atoms undergo then a sub-doppler cooling step in an optical molasses, followed by a magnetic trap with a time-orbiting potential (TOP trap), which allows for evaporative cooling of the atoms by lowering the strength of the TOP trap. In the final step the atoms are loaded into an optical dipole trap formed by two red-detuned, crossed and focused laser beams. The laser power is then reduced so that the atoms can further evaporate until we are left with the BEC. Adjusting the timing of this ramp allows us to vary the atom number. As the dipole laser we use the multimode Yb:YAG laser at 1030 nm , which is split to generate the so-called waveguide (WG), in which the atoms spread in longitudinal direction and the XDT (crossed dipole trap). After condensation, the dipole lasers can be ramped up again (usually only the waveguide) to load the BEC into the final configuration. For the quasi-1d confinement into the elongated trap we use $(\omega_{\parallel}, \omega_{\perp}) = (1.6, 160\text{Hz})$ [16] for the longitudinal and transverse trapping frequencies. A sketch of the final condensate is presented in fig. 3.1) and usually contains $\sim 10^4 - 10^5$ atoms in our BEC at a temperature of 20nK [38] .

3.1 Trapping and cooling

This section gives an insight into the working principles of two general concepts in the process of atom cooling and trapping, namely magnetic traps and optical dipole traps.

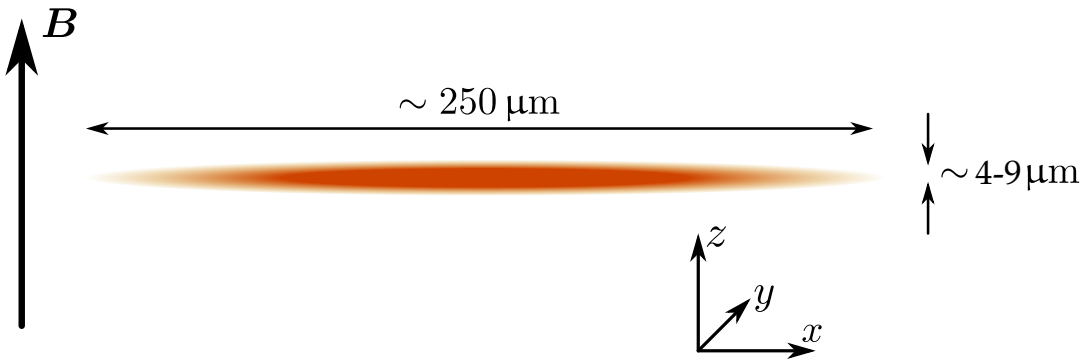

FIGURE 3.1: The final trap geometry of the waveguide provides an elongated condensate, tightly confined in transversal direction. Figure adapted from [39]

3.1.1 Trapping with magnetic fields

In our experiment we use magnetic fields in combination with lasers to generate the magneto-optical traps at the early stages of the cooling process. Yet another application is to combine magnetic fields with a time orbiting potential, generating an effective harmonic potential used as the first evaporation stage. This technique determines inherently the state in which we trap the atom. To arrive there one has to note that the coupling between a magnetic moment **m** and magnetic field **B** leads to the energy shift

$$\Delta E = -\mathbf{mB}. \tag{3.1}$$

The consequence is, that if the magnetic moment and the magnetic field are aligned parallel, the energy shift will be $\Delta E < 0$, so the atom will have its minimum energy in a high field. These atoms are called *high-field seeker*. If on the other hand the magnetic moment and field are aligned anti-parallel, the atom will have its minimum in a low field, since $\Delta E > 0$. This means that using harmonic potentials with a unique minimum as a magnetic trap (i.e. the TOP-trap in our experiment) solely catches the *low-field seeking* states. In our case we end with the atoms in the $m_{F=1} = -1$ state.

3.1.2 Dipolar forces

Optical dipole traps are important tools for cold atom experiments in general. Its particular importance for our experiment stems from the fact that by trapping atoms with them, the spin is kept as a degree of freedom, allowing us to do spin physics with the resulting BEC. Otherwise, the generation of the vector soliton would not be possible.

As mentioned before, we use them as a last stage of evaporative cooling as well as to load the BEC into the final geometry. But we can also utilise them to form vertical "barriers" and confine the BEC further in longitudinal direction. When describing dipolar forces conceptually, the dispersive interaction between the gradient of the light field and the dipolar moment **d** of the atom created by this light field is of interest - hence the name. The light field can be described by its intensity in terms of the electric field amplitude, $I = 2\epsilon_0 c|E|^2$. The dipolar force itself can be formulated as the gradient of an *interaction potential* as

$$F_{\text{dip}} = -\nabla U_{\text{dip}}(\mathbf{r}), \tag{3.2}$$

with the force acting towards the centre of the field for $U_{\text{dip}} < 0$, so in this case pushing the atoms into the intensity maximum, resembling the trap. In the opposite case, $U_{\text{dip}} > 0$, the atoms get pushed out of the field, corresponding to the barrier. The interaction potential comprises the coupling between the electric field and dipole moment and yields

$$U_{\text{dip}} = -\frac{1}{2}\langle \mathbf{dE} \rangle, \tag{3.3}$$

with the time average eliminating the rapidly oscillating terms. Following the calculations in e.g. [40] one arrives at an expression for the interaction potential in terms of the light field detuning $\Delta = \omega - \omega_0$ (ω_0: resonance frequency),

$$U_{\text{dip}}(\mathbf{r}) = \frac{3\pi c^2}{2\omega_0^3}\frac{\Gamma}{\Delta} I(\mathbf{r}). \tag{3.4}$$

Γ describes the on-resonance damping rate and originates from radiative loss of the system described by the Lorentz model. This treatment becomes important because the interaction between the light-field and atoms can be described semi-classically by the driving of a quantum mechanical two-level system. Hence, the previously excited atoms are able to re-emit photons, so to spontaneously decay into the ground state. Since these implications are not of further importance for this thesis, an extensive discussion is omitted. Looking at eq. 3.4 it becomes clear that choosing the detuning of our dipole laser appropriately, we can either create the trap by red-detuning ($\Delta < 0$) or the barrier by blue-detuning ($\Delta > 0$) the laser. Additionally, adjusting the intensity of the laser, we can deepen or flatten the potential, allowing it to be used for the evaporation of atoms and set the trapping frequencies.

3.2 Applying control over the system

After cooling the Rubidium gas we can employ different techniques to manipulate the internal states of the atoms. More precisely do we want to prepare different initial states, for example a polar state (see mean-field phase diagram fig. 2.4) or realise solitons experimentally. First the internal level structure of ^{87}Rb will be discussed, before presenting the different processes necessary to control these states.

3.2.1 Level structure of ^{87}Rb

The internal electronic groundstate can be either described in the fine structure picture, which results from the coupling of the electronic spin **S** and and its angular momentum **L** as

$$\mathbf{J} = \mathbf{L} + \mathbf{S}, \tag{3.5}$$

or in terms of hyper-fine splitting which couples the electrons total angular momentum to the angular momentum of the nucleus **I** as

$$\mathbf{F} = \mathbf{J} + \mathbf{I}. \tag{3.6}$$

Because of the low offset field in our experiment this is the appropriate coupling, so this work considers solely the latter picture. For ^{87}Rb the angular momenta are $J = 3/2$ and $I = 1/2$, resulting in the electronic groundstate $F = 1$ and $F = 2$, depending on whether they are oriented parallel or anti-parallel. Further it is worth to notice that every electronic angular momentum allows its corresponding magnetic moment to couple to an external static magnetic field, revealing the $2F + 1$ magnetic

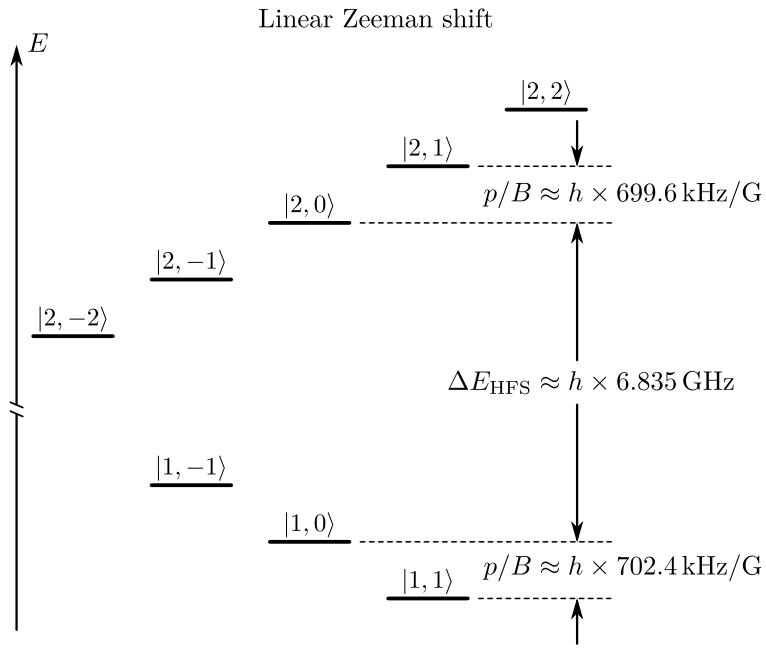

FIGURE 3.2: The level structure of the hyperfine manifolds $F = 1, 2$ including the respective energy spacings is shown. Due to the different signs of the g-factors, the levels are split in opposite order.

sublevels. For small fields this is the hyperfine structure equivalent of the linear Zeeman effect, which has been presented in eq. 2.13. Without external magnetic fields these levels are degenerate. For small energy shifts compared to the hyperfine splitting the interaction Hamiltonian for magnetic fields applied in the z-direction can be written as

$$H_B = \mu_B g_F F_z B_z, \tag{3.7}$$

with the Bohr magneton μ_B and the hyperfine Landé factor g_F. For ^{87}Rb the signs of g_1 and g_2 differ, inverting the energetic order of the magnetic sublevels in these two hyperfine manifolds as shown in fig. 3.2. The magnetic offset field used in our experiment responsible for this splitting is $B \approx 0.894G$, which is actively stabilised to a very high degree. A magnetic sensor is implemented close to the chamber which notices drifts of the magnetic field and feeds its signal into a PID loop. Temperature drifts on the scale of roughly one hour lead to a drift of the setpoint. To that end, a Ramsey spectroscopy is measured every hour, which uses the phase evolution of the atoms to monitor possible drifts in the magnetic offset field and to adjust the setpoint. The stabilisation process is crucial since the energy gap between the hyperfine levels depends on the strength of the magnetic field and therefore has an influence on the coupling between these states. All the states we are interested in can be prepared using solely the $F = 1$ manifold. However we do need the $F = 2$ manifold to be able to extract the desired observables (see section 3.2.5). A depiction of the level structure can be found in fig. 3.2.

3.2.2 Microwave fields

Microwave fields serve different purposes in our experiment. The relevant application for this thesis is use them for the transfer of populations between the two manifolds $F = 1$ and $F = 2$. This is particularly important for the implementation of the readout schemes described in 3.2.5. Both manifolds are separated by

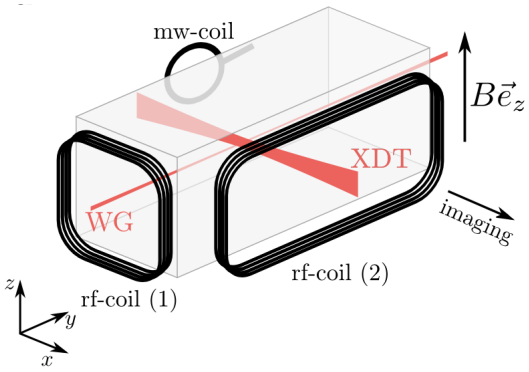

FIGURE 3.3: Sketch of the experimental setup including the glass cell with the crossed dipole lasers (XDT and waveguide) providing the final trapping geometry of the condensate, the mw-coil inducing transitions between the hyperfine manifolds F=1 and F=2 and the rf-coils, generating spin rotations and coupling the hyperfine levels m_F. Figure is adapted from [21].

an energy gap of $\sim$ 6.8GHz as shown in fig 3.2. The MW radiation includes all three polarisations necessary to couple the different Zeeman levels of both manifolds, $|F = 1, m_{F=1}\rangle \leftrightarrow |F = 2, m_{F=2}\rangle$ and hence couples all possible transitions. By tuning the frequency resonant to a desired transition we can drive solely this specific transition because the linear Zeeman shift is large enough. The coupling of two levels can be described using the two-level system and the spin-1/2 operators, where we effectively drive Rabi oscillations between the two levels. Adjusting the pulse duration allows us to precisely determine how much of the population we want to transfer, up to a total population inversion. This can be done very reliably.

3.2.3 Radio-frequency fields

We utilise magnetic rf-fields and pulses to mediate the transfer of atoms between the magnetic levels of a hyperfine manifold F. In that way we can induce spin rotations, mandatory for the generation of solitons (see sec. 5.1) and again for the implementation of the readout schemes (see sec. 3.2.5). In order to generate the required rf-fields a setup consisting of two magnetic coils is used (see fig. 3.3), where both separately can produce the needed oscillating magnetic fields. A detailed discussion and presentation of the rf-setup can be found in [21] and only the key ideas are discussed in the following. The oscillating fields are transversal to the offset field, hence the Hamiltonian governing this dynamic includes the linear Zeeman shift and the transverse rf-component, $\mathcal{H} = \mathcal{H}_B + \mathcal{H}_{\mathrm{rf}}$, with

$$\hat{\mathcal{H}}_B = \hbar\omega_{\mathrm{L}}\hat{S}_z \tag{3.8}$$

$$\hat{\mathcal{H}}_{\mathrm{rf}} = 2\hbar\Omega_{\mathrm{rf}}cos(\omega_{\mathrm{rf}}t + \phi_{\mathrm{rf}})\hat{S}_y. \tag{3.9}$$

The second Hamiltonian describes the effect of a linearly oscillating magnetic field $\mathbf{B} = B\cos(\omega_{\mathrm{rf}}t + \phi_{\mathrm{rf}})\mathbf{e}_y$ on the system and the rotation direction can be chosen to be around the $\hat{S}_x$-axis as well. As mentioned in section 2.3.2 the linear Zeeman term results in a Larmor precession around the magnetic field in z-direction with frequency ω_L. Transforming into the rotating frame of this system [41] allows us to get rid of

the time-dependence, i.e.

$$\begin{aligned}\hat{\mathcal{H}}_{\text{rot}} &= e^{-i\omega_{\text{rf}}t\hat{S}_z}\mathcal{H}e^{i\omega_{\text{rf}}t\hat{S}_z} \\ &= \hbar\Omega_{\text{rf}}[cos(\phi_{\text{rf}})\hat{S}_y - sin(\phi_{\text{rf}})\hat{S}_x] - \hbar\delta\hat{S}_z,\end{aligned} \tag{3.10}$$

where the detuning $\delta = \omega_{\text{rf}} - \omega_{\text{L}}$ has been introduced. To arrive at eq. 3.10 the quickly oscillating terms containing $2\omega_{\text{L}}$ are omitted in the rotating wave approximation. If we use a field resonant with the Larmor frequency , $\delta = 0$, the spin is solely rotated along a transverse axis, and the specific axis set by ϕ_{rf}. Equivalently, an off-resonant rf-field also maintains a rotation around $\hat{S}_z$.

3.2.4 Local Control

In addition to global spin rotation discussed before, we are also able to perform local spin rotations. To generate these local spin rotations we utilise a phenomenon generated by the interaction between the electric field of a laser and the atoms in our cloud, called Stark effect. The Hamiltonian can be written, following [16] and the derivation in [42] as

$$\hat{\mathcal{H}}_{\text{Stark}} = -\frac{1}{4}(\alpha_{\text{s}}(\mathbf{E}_1^*\mathbf{E}_2)\hat{\mathbb{1}} - \frac{i\alpha_{\text{v}}}{2F}(\mathbf{E}_1^* \times \mathbf{E}_2)\hat{\mathbf{F}}) \tag{3.11}$$

It comprises two terms, the scalar Stark shift and the vector-Stark shift and their respective scalar and vector polarisabilites α_{s} and α_{v}. Further, the classical electric field components $\mathbf{E}_j = E_j\boldsymbol{\mathcal{E}}e^{i(\omega t+\phi)}$ and the spin operator $\hat{\mathbf{F}}$ (see eq. 3.6) have been introduced. The scalar term can be used to derive a different picture of the dipolar traps, but is not of importance for the further discussion. Our laser can be assumed to be well aligned in the y-direction, hence the polarisation vector of the electric field is defined in transversal direction. The contribution of the vector Stark shift in eq. 3.11 acts like a fictitious magnetic field ([42], [43]) of the form

$$\mathbf{B}^{\text{fict}} = \frac{i\alpha_{\text{v}}}{8\mu_B g_F F}(\mathbf{E}_1^* \times \mathbf{E}_2). \tag{3.12}$$

and is not solely an effect of the light-field but emerges merely from its interaction with the electric dipole of the atom. Although called fictitious magnetic field, it is as real as any other magnetic field, just that it is created by a laser. The fictitious field is parallel to the propagation of the light and adds vectorially to the magnetic offset field, aligned in z-direction. Since this effect is sufficiently small, it can be neglected here. By choosing equally circularly polarised light for co-propagating field components, the amplitude of this fictitious field is maximised. By inserting the expressions for the electric fields in eq. 3.12 we can rewrite it to

$$\mathbf{B}^{\text{fict}} \propto (E_1^2 + E_2^2 + 2E_1E_2cos(\Delta\omega + \Delta\phi))\mathbf{e}_{\text{y}}, \tag{3.13}$$

[16]. The phase difference $\Delta\phi$, as well as a the frequency difference $\Delta\omega$ can be accomplished technically by an amplitude modulation of the local control laser, which results in different frequency components for the electric field components. The fictitious field decomposes now into a static term $\mathbf{B}_0^{\text{fict}}$, originating from the first two terms in eq. 3.13 and an oscillating term $\mathbf{B}_{\text{rf}}^{\text{fict}}$. The oscillation frequency is determined by the frequency difference of the electric field components $\Delta\omega$ and when chosen at the Larmor frequency the resulting magnetic field can be utilised to induce transitions similar to the rf-transitions discussed in sec. 3.2.3. The important

difference here is though, that the rf-coupling of the m_F-levels is spatially localised, hence the name local spin rotation. Intuitively, one can think of this process also as a Raman transition of the atom via an virtual state.

An illustration of the optical and laser setup essential for the local rotations can be found in fig. 3.4. For the laser we use the DL pro from Toptica, which allows us to set its wavelength to 790 nm, tuning out the scalar Stark-shift [44], and leaving solely the vector Stark-shift in order to generate local spin rotations. In order to stabilise the laser's intensity a PID control loop is used which adjusts the RF signal of the acousto-optic modulator (AOM). To do so the beam gets fed into the loop by partially directing it to a photodiode and a sample-and-hold (S&H) circuit ensures that the regulated power gets applied during the next cycle. The AOM can also serve as a switch turning the beam on the atoms on and off and additionally modulates the beam amplitude at the Larmor frequency ω_L by generating side-modes in the frequency spectrum at $\pm\omega_L/2$. For the modulation we use different arbitrary wave generators (AWGs). They allow us in general to use arbitrary functions and frequencies in a range of applications and play a crucial role when it comes to driving the AOM and crossed AODs in front of the experiment. The necessary electronic signal path to drive the AOM to our needs can be seen in fig. 3.5. Afterwards the laser gets coupled into a fiber and is polarisation cleaned by a partial beam splitter (PBS) before it is send to the AOD setup in front of the experiment, where the laser is steered onto the atom cloud.

3.2.5 Accessing spin observables and imaging

For the experiments discussed in the later chapters the main interest lies in extracting the spin information of our system. The F_z component is easily accessible, since the alignment of the magnetic offset field is chosen in z-direction and hence naturally inherits this information. Calculating it from the level populations in $F = 1$ yields

$$F_z = \frac{N_{+1} - N_{-1}}{N_{\text{tot}}}. \tag{3.14}$$

After we employed the necessary rotations in order to map the desired spin observables we turn off the trap, use a Stern-Gerlach magnetic field gradient with a 2 ms time of flight to spatially separate the magnetic hyperfine states m_F and apply high-intensity absorption spectroscopy to image the atom cloud. Further details on the method and calibration can be found in e.g. [45] and [46]. We first image the $F = 2$ manifold by applying a 15 µs pulse of resonant light via the D_2-line. After a 1 ms gap, the atoms in $F = 1$ get imagined utilising the same state as before. In that manner the different levels are imaged consecutively onto a CCD. As a part of the imaging process the photons get scattered or absorbed by the cloud, so the result is basically the shadow viewed from the opposing side, where the density can be calculated from the opacity of the cloud. Consequently, every imaging process destroys our condensate, encapsulating quantum mechanics notion that we can not measure and simultaneously preserve the system. From that we can extract the 1d densities of the atoms in x-direction on one pixel in each hyperfine level and use them for the calculation of the observable in e.g. eq. 3.14. The CCD contains 5 pictures, of which two are the images containing atoms. For both hyperfine states a reference picture with no atoms is taken. These are used later for the processing of the data to reduce the imaging noise and remove fringes on the pictures (see appendix B).

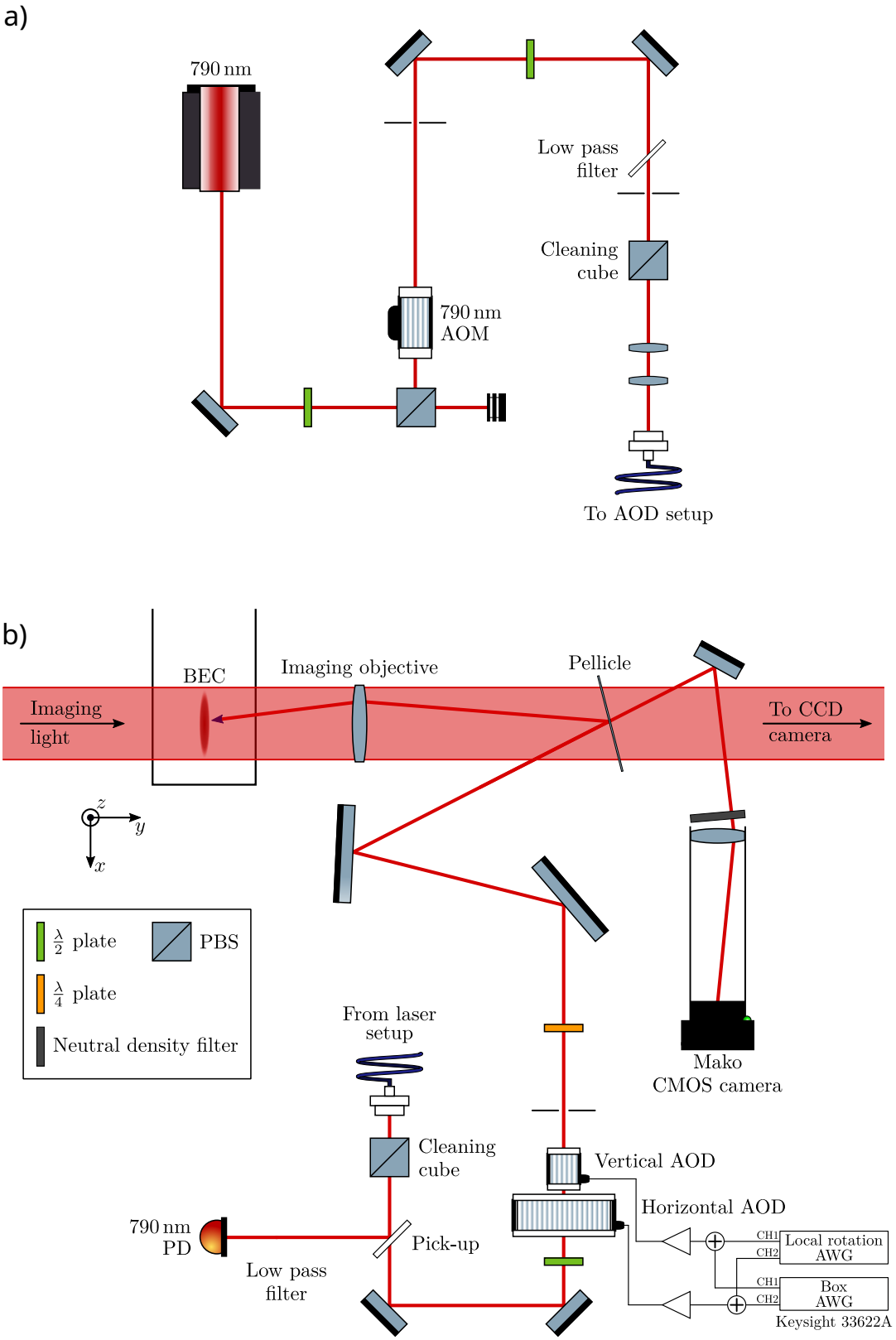

FIGURE 3.4: Optical Setup for the generation of local spin rotations with a) the AOM buildup for the generation of a power stabilised beam and b) the alignment in front of the glass cell. Figure is adapted from [16].

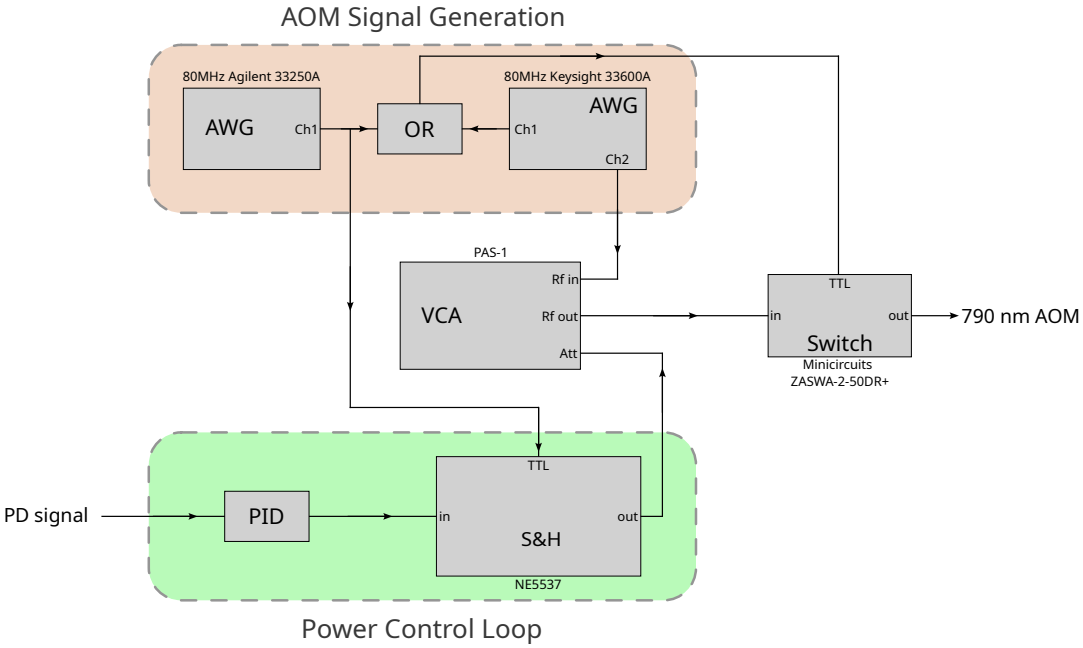

FIGURE 3.5: Signal path necessary for the AOM modulating the incoming beam with the Larmor frequency ω_L. The signal entering the control loop is regulated by a PID to a setpoint of 6.5 V and fed into the sample-and-hold (S&H). The AWG signal timing is chosen such that the signal is fed for the next experimental cycle as the attenuation level into the voltage controlled amplifier (VCA).

Chapter 4.

Noise Reduction of local spin rotations

At the heart of ultracold atom physics lies the ambition to reveal and probe quantum mechanical processes. One such process is prominently represented by the presence of quantum correlations which is a precursor for the stricter condition of entanglement between quantum objects. The challenge of observing quantum correlations in any experimental system lies in the fact that the scales on which they are expected to occur are notoriously small and usually overshadowed by classical contributions, such as thermal fluctuations or imaging noise. Aiming at the study of solitons, the setup used for their generation, i.e. the local rotation setup, therefore has to guarantee a minimal contribution of such classical fluctuations and a reproducibility of the generated state. This chapter will present an approach to effectively reduce the fluctuation level close to the classical limit imposed by a coherent state in section 4.1. Afterwards, the stability of the rotation angle will be investigated shortly and a model for the characterisation of the shot noise limit will be discussed in sec. 4.2. Additionally, a post processing routine is implemented in sec. B to eliminate the statistical noise originating from the imaging. Finally, the comparison of the experimental data with the theoretical expectation is then presented in 4.2.4.

4.1 Technical realisation

4.1.1 How to broaden the effective laser beam on atoms

The question of how to reduce noise in the preparation of solitons is deeply linked to the question of how to reduce the noise for local rotations in general. The necessity to look at this step in our experiment became clear in [16], where the fluctuations in the rotation amplitude, after rotating the initial state $|1,-1\rangle$ with a $\pi/2$-pulse, was investigated. A $\pi/2$ pulse transfers the state into the transverse spin plane of the spin sphere, where the average spin in z vanishes, $\langle F_z \rangle = 0$, but their fluctuations reach a maximum. If the rotation amplitude fluctuates, the final state fluctuates around the ideal $\pi/2$ rotation state. In addition to this empiric approach, a more systematic approach has been conducted to reveal the different noise sources, determine the component with the highest impact and develop a scheme to reduce it in our system [47]. The main focus was put on the comparison between intensity fluctuations of the local rotation laser and positional fluctuations. It was found that the positional fluctuations are the dominant source, which originate from the relative motion between the Gaussian beam of the laser and the condensate in vertical direction. This can emerge due to thermal drifts or vibrations in the optical setup. The optical setup is presented in fig. 3.4 and is in its construction identical to the ones used in the before mentioned works. The two acousto-optic deflectors (AODs) at the end of the

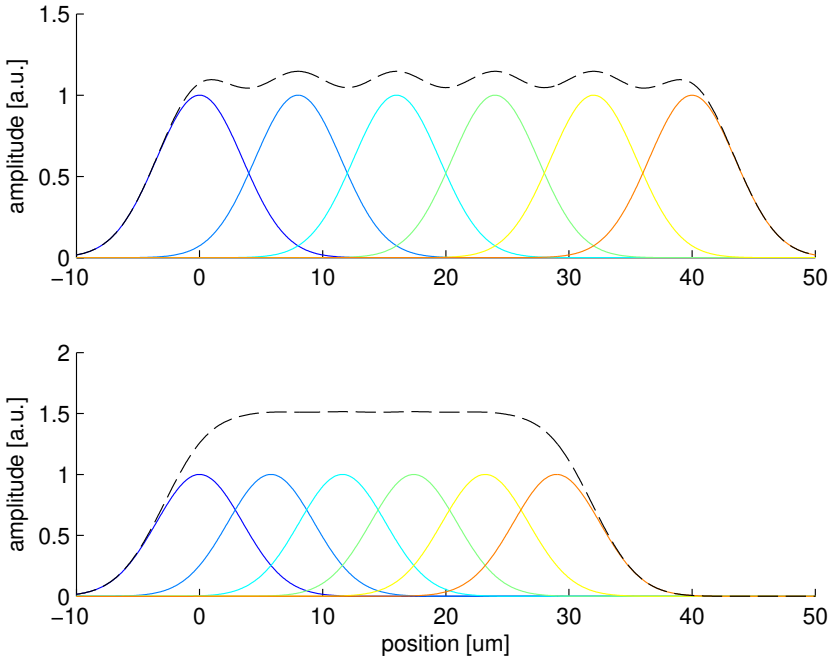

FIGURE 4.1: Rough illustration showing the sum of overlapping Gaussian functions. The width corresponds to the RMS width of $\sigma = w/2 = 3.5\,\mu m$ of the Gaussian beam used in the experiment. In the upper row, the distance between the Gaussian functions is chosen to $8\,\mu m$, for which the combined profile contains small "wiggles". By adjusting the distances to $\sim 5.8\,\mu m$ a seemingly flat profile is obtained.

path are used to enable control over the horizontal and vertical position of the beam, respectively. In AODs, an incoming laser beam gets deflected by a sound wave, which is generated by a RF-driven piezo actuator into a crystal. The scattering angle then depends on the frequency of the sound wave [48], which we can control externally (see sec 3.2.4). Hence, the laser can be steered by changing the piezo frequency. With this in mind the approach has been to artificially broaden the beam by using a frequency ramp with the vertical AOD. It was shown that this scheme reduced fluctuations in F_z, whereas the comparison to the coherent state fluctuations revealed still a high deviation (factor 10) from this quantum limit.

The problems in the original setup might occur due to the different rotation amplitudes induced by spatial profile of the laser, originating from the flanks of the Gaussian function. The implemented frequency sweep in vertical direction has been found to result just in a broadened Gaussian profile, originating from a smoothly peaked *Gaussian* beam. Hence modulating the beam in that manner still maintains its flank structure. Sweeping the AOD frequency can further result in interference between two beams which originate from a simultaneous deflection of the incoming beam at different angles. The approach chosen in this thesis here is to modulate the vertical AOD with pulsed frequencies, rather than sweeping it. The advantage here lies in the fact that we overlap several Gaussian beams at different positions, theoretically resulting in a profile resembling approximately a plateau or *rectangular function* over an extended spatial area, rather than a Gaussian (see fig. 4.1). On the edges we still obtain Gaussian flanks, but we can suppress their effect by setting the plateau wide enough. To do so, a frequency interval $[f_c - \Delta f, f_c + \Delta f]$, symmetric

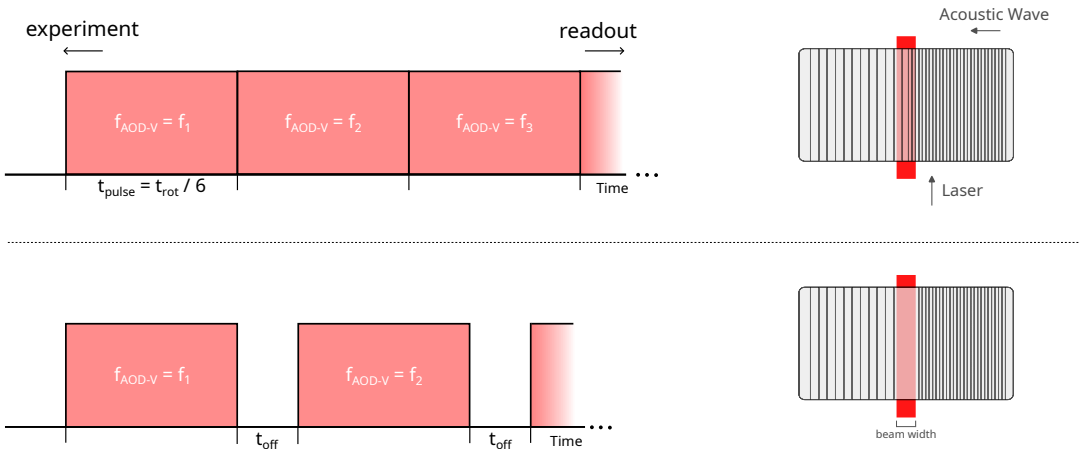

FIGURE 4.2: Upper row: The pulse timings to generate consecutive laser pulses in vertical directions are shown. The modulation width Δf and number of pulses N_{pulse} define the frequency spacing through $\delta = 2\Delta f/(N_{\text{pulse}} - 1)$. The right figure sketches the overlap of the laser passing through the AOD and two sound waves of different frequencies, if the pulses are applied without a buffer time.
Lower row: The pulse timings as discussed in sec. 4.1.3 are shown. An additional AOD buffertime is used to prevent the simultaneous overlap between two sound waves and the incoming beam. A sketch is shown on the right.

around the vertical frequency of the "best" overlap f_c, is divided into 6 equidistant steps with a frequency spacing of $\delta f = 2\Delta f/5$. The quantity Δf will be referred to as modulation width in the following. The specific frequencies used for the vertical deflection are then calculated by

$$f_m = f_c - \Delta f + m\delta f, \tag{4.1}$$

with $m = [0, .., 5]$. To keep the total rotation time fixed to a desired value t_{rot}, we divide it into 6 equal steps as well, so $t_{\text{pulse}} = t_{\text{rot}}/6$. The sketch of the pulse sequence is shown in fig. 4.2 in the upper row.
This process is comparable to modulating the AOD's signal directly, in order to get a rectangular function by choosing an appropriate RF signal. To find this function the convolution between the incoming Gaussian beam b and the AOD signal s must be considered. The rectangular function is then calculated by the time Fourier transform of this convolution, $rect = \mathcal{F}(s * b)$. The rectangular function is then obtained by applying a sinc-function driving the AOD. Only the sinc-modulation of the AOD would eliminate the Gaussian flanks and result in a *rectangular* function. Yet another approach would involve the application of e.g. cylindrical lenses.

4.1.2 Calibrating the vertical AOD's frequency modulation

Implementing the previously introduced pulse sequence requires a calibration of the spatial pulse separation, to ensure a plateau-like structure is achieved, while the dips in between the peaks are minimised "sufficiently". This is done using the frequency modulation in horizontal direction, since only in this case we are provided with a spatial profile of the different pulses on the atoms. Assuming that the AOD fluctuations can be treated equally in vertical and horizontal directions allows us to transfer the frequency calibration to the final vertical modulation. The approach is to measure the 6-pulse scheme in different configurations of Δf, to allow for an estimation of the spatial shift of the Gaussian peaks. We want to determine a relation between the frequency difference $\delta f = f_i - f_j$ and the distance between two local rotation peaks, to be able to later tune in a desired distance by adjusting the frequency spacing in the AOD signal. As a measure we therefore use the change in the distance between two neighbouring peaks,

$$d_{ij}(\delta f) = |x(f_i) - x(f_j)|, \tag{4.2}$$

where $f_i = \{f_1, ..., f_6\}$ $(i \neq j)$ are the different frequencies used in the AOD to shift the beam along the cloud and generate the 6 pulses. The absorption images are shown in fig. 4.3. Using the average distance for each Δf, we show also in fig. 4.3 that a linear dependence emerges between the distance and frequency spacing. The slope defines the rate at which the distance changes with δf and provides a tool to adjust the distance freely. The rate we obtain from a linear fit is

$$\delta d = 94.1 \frac{\text{px}}{\text{MHz}} = 39.5 \frac{\mu\text{m}}{\text{MHz}}, \tag{4.3}$$

where a $1\text{px} = 0.42\,\mu\text{m}$ was used, to obtain the latter expression. This size corresponds to the pixel size at the position of the atoms. Aiming at reducing the wiggles on the profile to 1% we must choose a frequency spacing resulting in a peak-to-peak distance of $d_{pp} = 5.8\,\mu\text{m}$[1]. This gives us finally a frequency spacing of

$$\delta \bar{f} = \frac{d_{pp}}{\delta d} = 0.147\,\text{MHz}. \tag{4.4}$$

Using this frequency spacing gives us the modulation width $\Delta f = 0.368\,\text{MHz}$. Applying it in horizontal direction results in a profile, which still consists of small wiggles but otherwise resembles the desired flat profile over an extension of $\sim 20\,\mu\text{m}$, which exceeds the vertical extension of the cloud by factor of 2 (see horizontal application in fig. 4.4) and is thus applied for the vertical frequency modulation in the next step. The beam width extracted indirectly through the rotation profile is larger compared to the actual beam width of the laser. This originates most likely from an expansion induced by the repulsively interacting atoms during a short time of flight phase between the pulse and imaging ([16], [49]). It can also be seen that we can not reach the maximum transfer fraction of the local spin rotation, i.e. $F_{z,max} < 1$. This can be explained by the presence of the static offset field due to the laser, effectively tilting the axis on which the observable is projected. A comparison with [16] shows a good agreement with the calculated transfer fraction of ~ 0.9. There, the signal was modulated with a square wave function though, whereas in our case we used a sine-modulation. Further, the horizontal profile must be taken with caution and is just a visualisation of the indeed flattened *and* broadened profile, since we do not have any

[1] This value was estimated varying the peak distances in the model shown in fig. 4.1

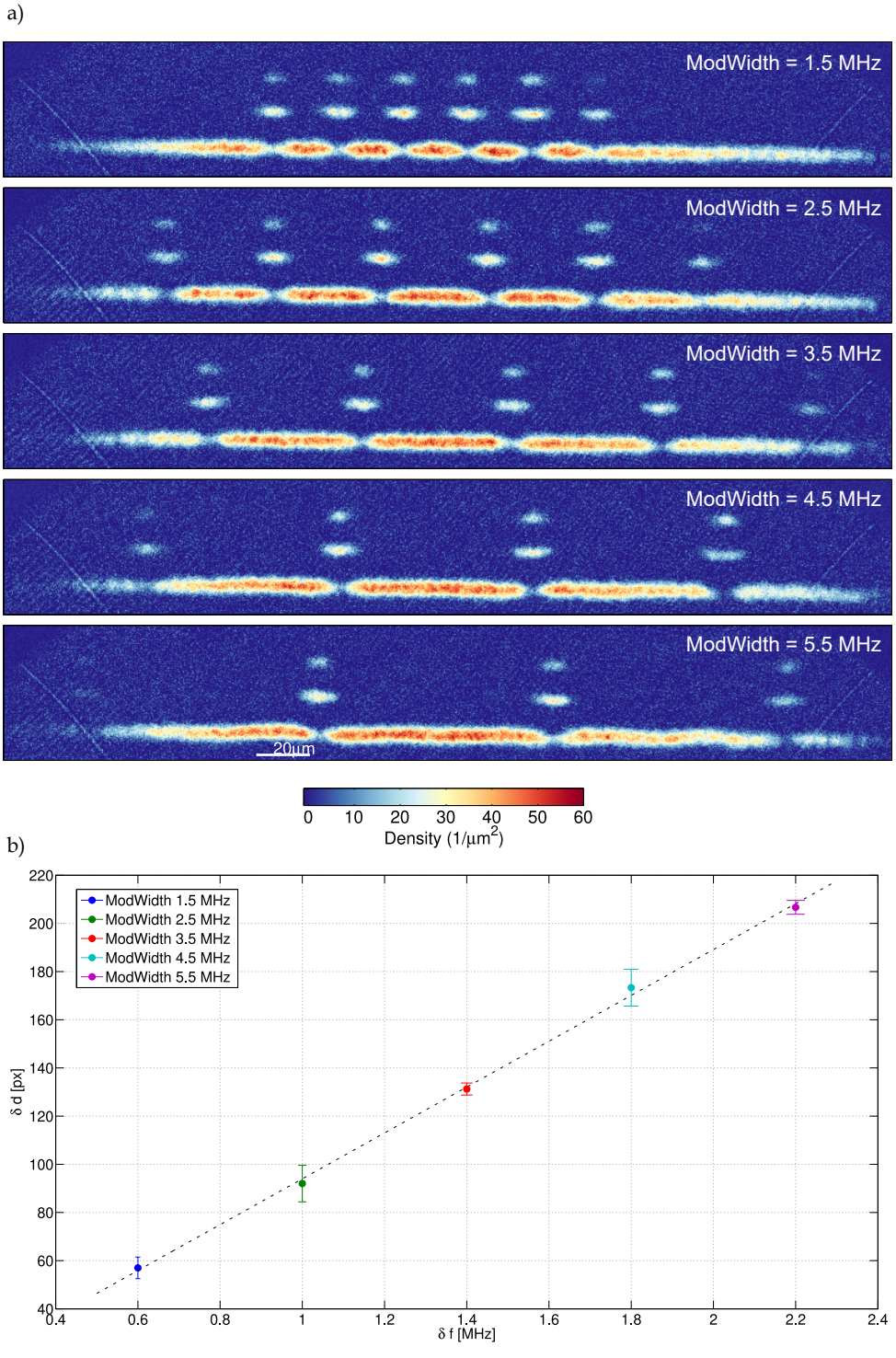

FIGURE 4.3: a) The absorption images of the 6 pulses in horizontal direction with increasing modulation width Δf are shown. The peak positions for each setting have been extracted.
b) The distances between the peaks for different frequency spacings Δf were used for a linear fit to estimate the step size $\delta f = 2\Delta f/5$ needed to set a certain spatial separation of the different beam pulses. To this end the slope $m = 94.1 \frac{\text{px}}{\text{MHz}}$ was used .

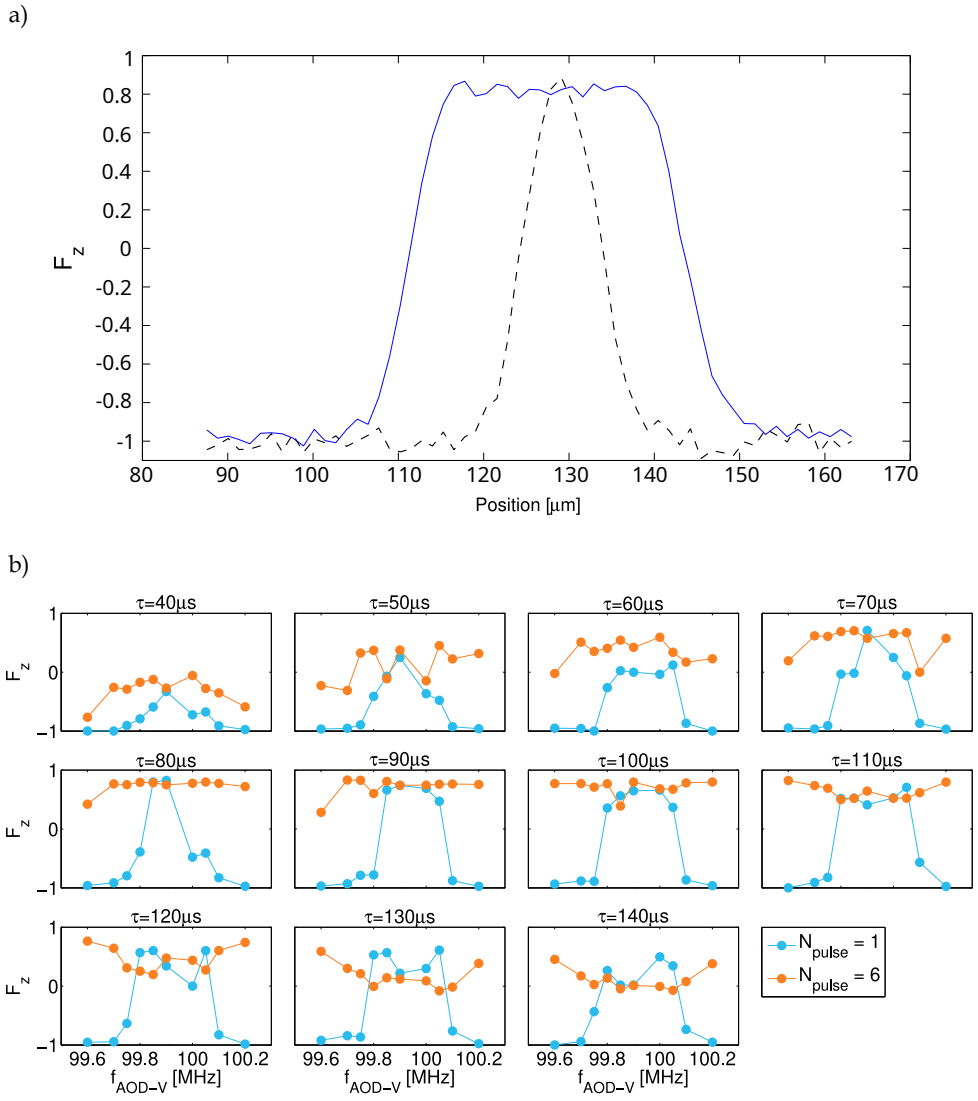

FIGURE 4.4: a) Comparison between a single beam centered (dashed black line) on the condensate and the 6 beams (blue line) applied in horizontal direction with an $t_{\mathrm{rot}} = 80\,\mu\mathrm{s}$. Pulsing the beam results in a profile which extends its maximum to a plateau ranging over $\sim 20\,\mu\mathrm{m}$, whereas the single beam shows a narrow maximum with prominent Gaussian flanks. b) The spin rotation amplitudes for the new scheme applied in vertical direction and for increasing rotation time show the emergence of a broader flattened profile in the case of 6 consecutive beams. Due to the increased strength the rotation back to the initial state starts at earlier rotation times.

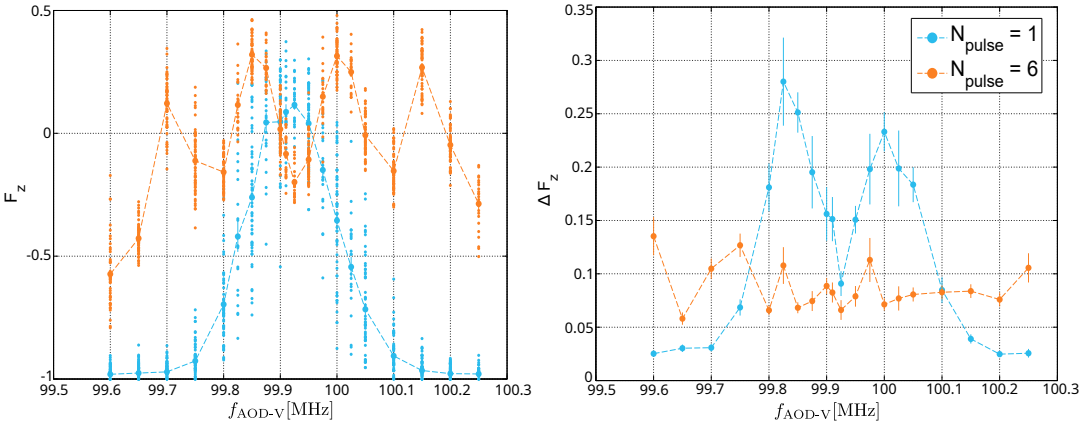

FIGURE 4.5: Left: The rotation amplitudes in the F_z profile for different center frequencies $f_{\mathrm{AOD-V},0}$ for 6 beams and one beam are compared. Although the new rotation scheme broadens the profile, an amplitude modulation, i.e. spike structure, can be seen. This originates from interference between two consecutive AOD frequencies and the laser. The wiggles lead to fluctuations on the scale of 30% around the anticipated value $F_z = 0$.
Right: The fluctuations, given as the standard deviation, can be reduced to a consistent level over an extended area compared to the level of a well-aligned single beam and even slightly below at the point of best overlap with the condensate ($f_{\mathrm{AOD-V}} \approx 99.9\,\mathrm{MHz}$). For $f_{\mathrm{AOD-V}} < 99.75\,\mathrm{MHz}$, the fluctuations caused by the single beam reduce strongly, because it does not overlap with the condensate anymore.

control of the vertical positional fluctuations in this scenario. It must also be noted that the results were obtained from a manual estimation of the peak positions at that time. A more precise analysis would involve the fitting of Gaussian functions to the density profiles, in order to extract the peak positions more accurately.

In the next step we compared the local rotation profiles between the newly implemented rotation scheme and a single centred beam. For this measurement we performed the local spin rotations on the atoms sitting in $|1,-1\rangle$, so starting with an aligned spin $F_z = -1$. Applying a $\pi/2$- pulse rotates the spin into the transverse plane where F_z vanishes and consequently a π-pulse results to $F_z = 1$. To show the effectiveness of this scheme, we measure the spin rotation amplitudes for different frequencies of the vertical AOD $f_{\mathrm{AOD-V}}$. This means we use a different vertical position of the single beam with a frequency f_c and apply then for each f_c also the 6 beams modulation. Its extended profile should now compensate the poorly aligned position of the single beam, where it just partially overlaps with the condensate, still providing us with a high amplitude. In fig 4.4 we measured the rotation amplitude for different rotation times.[2] An increasingly flatter profile is indeed observed as anticipated, where a high rotation amplitude can be seen over an extended frequency space. At $f_{\mathrm{AOD-V}} = 99.9\,\mathrm{MHz}$ also the single beam reaches a maximum rotation

[2]The power of the vertical AOD is set to $P_{AOD} = 0.38\,\mathrm{V}$ for the single beam and $P_{AOD} = 0.8\,\mathrm{V}$ for the 6 beams as amplitudes of the signal coming from the function generator, to obtain a similar rotation angle in the region of best overlap between the single beam and condensate. The signal then passes a switch and is amplified before entering the AOD.

amplitude due to its good overlap with the condensate. For $\tau > 110\,\mu s$ the amplitude obtained from the 6 separate rotations declines and falls below the case of just one beam. The higher rotation power results in an earlier rotation back to the initial state, corresponding to a rotation angle $\alpha > \pi$. In fig. 4.5 a rotation time of $\tau = 46\,\mu s$ is chosen, which resembles approximately the $\pi/2$-rotation. Although the effective vertical region of spin rotations increases, we observe a spike structure around the intended amplitude $F_z = 0$. The amplitude F_z spans a range of $\Delta F_z \approx 0.6$. A detailed discussion and solution is presented in sec. 4.1.3. The effect on the fluctuation of the local rotation is visualised in fig. 4.5. As anticipated, we can reduce the fluctuations in case of the 6 beams slightly below the value originating from a single well-aligned beam over a larger frequency range.

4.1.3 Preventing interference between AOD pulses

So far, the signals for the AOD, steering the beam vertically, have been set without considering any relaxation times for the crystal. A problem originating from this is the simultaneous overlap between the laser light, passing through the AOD, with the already passing wave, as well as the newly incoming wave. As a consequence the laser would get deflected partially in two different but similar angles, resulting in an unwanted simultaneous spin rotation of the atoms at different positions with hardly controllable amplitude. Further, the deflected beams can overlap and interfere destructively, which could inflict a modulation of the rotation spectrum. To avoid this effect, we therefore want to ensure that the preceding sound wave fully traversed the beam (see sketch in fig. 4.2 on the right). As an initial rough estimation of the needed AOD buffer time we use the propagation speed of the acoustic wave and the size of our laser beam. Since it fills out the aperture of the AOD built into our setup [49] we can use its aperture size for this calculation. We use the 2-axis shear mode AOD DTSXY-400-780 from AA Opto-Electronic, which provides us a shear mode velocity of 650 m/s. The beam-width of the laser after the fibre coupler is $b_w = 3.88\,mm$. To ensure that a wavepacket fully traversed the beam, the aperture size, $s = 4.2\,mm$ is used. Hence the needed time calculates to

$$t_{off} = \frac{s}{v_{shear}} = 6.5\,\mu s. \tag{4.5}$$

This value can be compared to the results obtained from experimentally testing different buffer times. For the implementation of the buffer-time into our pulse scheme, the time interval for each local rotation pulse was extended by t_{off}, to ensure that the total effective spin rotation time remains preserved (see lower row in fig. 4.2). The total rotation time is now

$$t_{tot} = 6(t_{rot} + t_{off}). \tag{4.6}$$

In fig. 4.6 the Fz amplitude for a $\pi/2$ rotation and different buffer times is shown. We see that the modulation of the profile gets seemingly reduced for an increasing buffertime. Following these result we set the buffertime according to the calculated value of 6.5 µs for the following measurements. For frequencies $f_{AOD-V} > 100\,MHz$ the overlap between the extended profile and the condensate reduces , resulting in a reduced amplitude. Nevertheless, the obtained values for the amplitude extend over a range of 0.15 in the analysed frequency interval, or 7.5% of the entire range.

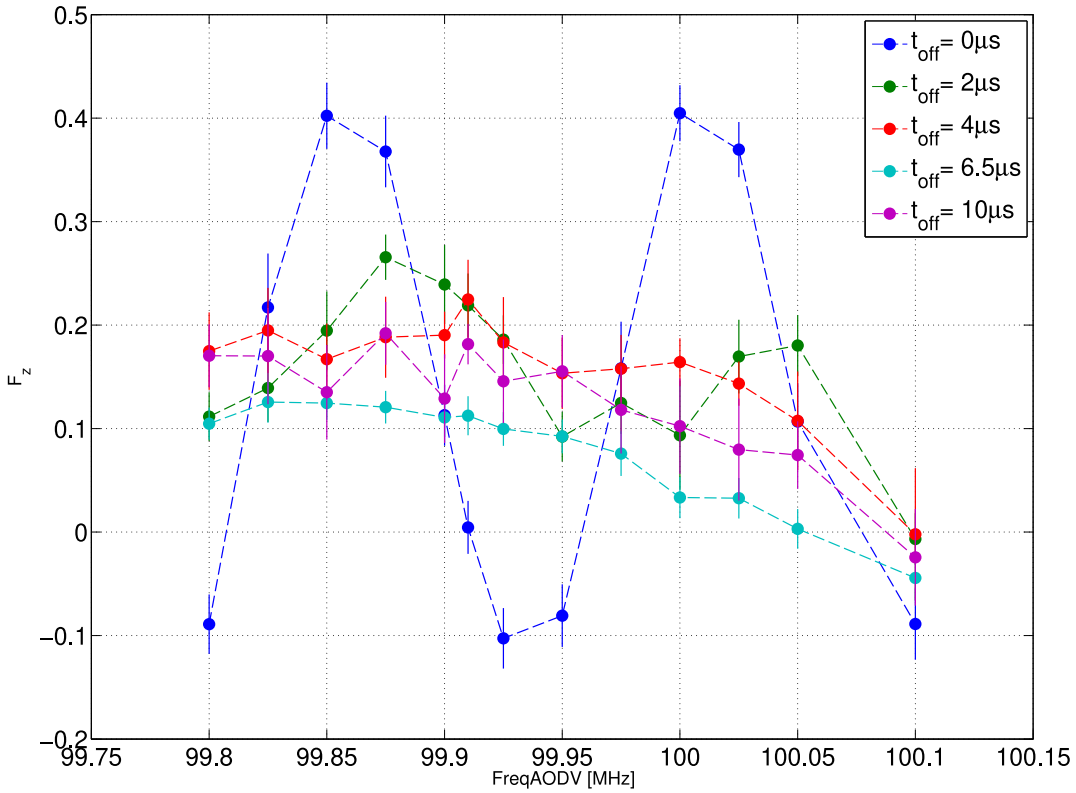

FIGURE 4.6: Introducing a buffer time for the vertical AOD to allow the sound wave to fully traverse the incoming laser reduces the modulation of the F_z profile and flattens it over an extended frequency range. Further, the amplitude is reduced from s span of ~ 0.5 in the case of no buffertime to span ~ 0.1 in the case of $t_{\text{off}} = 6.5\,\mu\text{s}$.

4.2 Characterising the noise of local rotations

The following sections aim towards characterising the noise exerted by the new local rotation setup and to reveal how strong the measured fluctuations deviate from the ideal case of a coherent spin state. To do so, the stability of the rotation angle will be discussed briefly, since strong fluctuations in the rotation amplitude would translate into an insufficient reproducibility of the anticipated state. More emphasis will be put further on analysing the fluctuations of the F_z spin observable. To do so the quantum limit of the coherent spin state will be considered as a baseline to which the experimental data, obtained with the new pulse scheme, will be compared. For the results discussed below, an optimal reference picture analysis was performed (see appendix B) to further reduce noise caused by the imaging and fringes.

4.2.1 Coherent Spin States

To develop a model of the measurement statistics and thus the expected shot noise limit we consider the case of an initial coherent state, in which each atom is prepared in the same quantum state and fluctuates independently. We will use these states throughout the next chapters as a reference to compare the measured fluctuations to.

Coherent states contain the important feature of representing a minimum uncertainty state, i.e. they fulfil the minimum uncertainty relation $\Delta^2 A \Delta^2 B = \frac{1}{4}|\langle [A, B] \rangle|^2$, here written in terms of two general conjugate observables A and B, hence makes them a well-suited measure for the standard quantum limit. Assuming that after a local rotation the character of a coherent state is satisfied, i.e. each atom is rotated individually, we aim to calculate how far the measured fluctuations diverge from the expected fluctuations.

To gain a better picture, we can determine the coherent states on the spin sphere, i.e. its extension due to the natural uncertainty of its spin observables. The only relevant spin observable in this thesis is F_z, hence the further process will focus on deriving fluctuations of the combined variable $N^- = N_{+1} - N_{-1}$. Based on the derivation for general combined variables of this type given in the appendix A.1, the fluctuation is given by the variance,

$$\Delta^2 N^- = N, \tag{4.7}$$

and after a normalisation with the total atom number, yields

$$\frac{\Delta^2 N^-}{N} = 1. \tag{4.8}$$

The equivalent result is obtained for the conjugate spin variables F_x or F_y. Moving to the normalised standard deviation we obtain

$$\frac{\sqrt{\Delta^2 N^-}}{N} = \frac{1}{\sqrt{N}}. \tag{4.9}$$

The coherent state and its uncertainty are hence represented on the spin sphere as a disk with radius $1/\sqrt{N}$. Consequentially, the size of this state shrinks with an increasing atom number.

4.2.2 Rotation Amplitude

The stability of the local rotation setup can be first characterised by answering the question of how reproducible the prepared state is. An important quantity to analyse is the rotation angle α. Intuitively, the rotation angle can be thought of as the angle at which an initial state is rotated on the spin sphere. We can describe a general rotation of a state $|\psi\rangle$ by considering the time evolution operator $\hat{U} = e^{-i\Omega(x)F_y t}$, with a spatially varying Rabi frequency $\Omega(x)$. The rotation is performed around the F_y axis but could have been chosen as well around any arbitrary axis in the $F_x F_y$ plane, due to the rotational symmetry of the spin sphere. The expectation value of the F_z spin for a state prepared in $|1,-1\rangle$ is in every case the same and calculated via

$$\langle F_z \rangle = \langle \psi | \hat{U}^\dagger F_z \hat{U} | \psi \rangle. \tag{4.10}$$

Evaluating this expression, presuming a Gaussian Rabi frequency profile, i.e. $\Omega(x) = \Omega_0 e^{-x^2/2\sigma^2}$ unfolds the F_z projection to be intrinsically linked to the rotation angle $\alpha = \Omega_0 t$ as

$$\langle F_z \rangle = -\cos(\alpha e^{-\frac{x^2}{2\sigma^2}}), \tag{4.11}$$

with a RMS beam width $\sigma = w/2 = 3.5\,\mu\text{m}$ (here chosen in 1D). Focussing on the maximum amplitude, the Gaussian function takes on the value of 1. In this case, we determine the fluctuations in the rotation amplitude and hence rotation angle via

$$\Delta^2 \alpha = \Delta^2(\arccos(F_z^{max})). \tag{4.12}$$

In fig. 4.6 the fluctuations of the rotation amplitudes, hence angles, are given as the standard deviation on each averaged data point, $\sqrt{\Delta^2 \alpha}$. Experimentally, we prepared roughly $\pi/2$ rotations with $\tau = 46\,\mu\text{s}$. In the case of the buffertime $t_{\text{off}} = 6.5\,\mu\text{s}$ and over the range of different $f_{\text{AOD}-\text{V}}$ ($\sim 0.3\,\text{MHz}$) we obtained fluctuations of the rotation angle in a range of $4.6 - 6.9°$, and on average at $\sqrt{\Delta^2 \alpha} = (5.62 \pm 0.84)°$. For this measurement we analysed though only $\sim$ 30 realisations for each vertical AOD frequency showed in fig. 4.6. Measuring more realisations for one AOD setting could further improve the precision of this result.
To get an idea whether the fluctuating rotation amplitude impacts the prepared state on relevant scales, we can compare it to the size of the coherent state. Its extension, when normalised to the total atom number, is given by the standard deviation $\sigma = 1/\sqrt{N}$ as the disk radius. (see sec. 4.2.1). So to calculate the opening angle, we take advantage of the normalised radius of the spin sphere and obtain for the entire extension $\tan(\gamma/2) = \sigma/1$. For this case, we use the average total atom number at the point of the amplitude, $N \approx 339$, and estimate an average total extension over all shots of $\sim 6.2°$. Considering only the absolute value of the rotation amplitude fluctuation, it falls below the extension of the coherent state. So it can be said that the state is prepared inside the disk of a perfect $\pi/2$ rotation. However, the error on $\sqrt{\Delta^2 \alpha}$ exceeds the disk slightly. Including the extension of the coherent state increases the size of the expected state by a factor ~ 2 in the F_z direction.

4.2.3 Estimating the quantum limit for F_z

As introduced in 2.2 a single particle quantum state can be formulated using the magnetic hyperfine states as

$$|\psi\rangle = a|+1\rangle + b|0\rangle + c|-1\rangle. \tag{4.13}$$

The coefficients carry the information about the probability of an atom populating the respective state, $p_{+1} = |a|^2$, $p_0 = |b|^2$, $p_{-1} = |c|^2$. Extending this to the many-body case and describe coherent states, we can use product states of the form $|\psi_{\text{ges}}\rangle = |\psi\rangle^{\otimes N}$. If we want to calculate the probability of a certain configuration of the atoms over the three magnetic levels has we can use the trinomial distribution with probability mass function [50]

$$P(N_{+1}, N_0, N_{-1}) = \frac{N!}{N_{+1}!N_0!N_{-1}!} p_{+1}^{N_{+1}} p_0^{N_0} p_{-1}^{N_{-1}}. \tag{4.14}$$

The fluctuations are determined by the variances

$$\Delta^2 N_i = N p_i (1 - p_i). \tag{4.15}$$

Experimentally, the probabilities p_i are accessed using the populations of the different levels relative to the total atom number $N = N_{+1} + N_0 + N_{-1}$ as

$$p_i = \frac{N_i}{N}. \tag{4.16}$$

Since we want to use the local rotations to generate solitons and aim to analyse the spin observables, it is meaningful to consider in the following the unnormalised F_z-spin projection

$$F_z = N_{+1} - N_{-1}, \tag{4.17}$$

as introduced in sec. 3.2.5, instead of the atom number fluctuations themselves. Here the normalisation with the total atom number averaged over all realisations $\bar{N}$ is used to ensure the single shot fluctuations are eliminated and to achieve a value comparable to the coherent state. The variance of this quantity is then formulated as

$$\begin{aligned} \Delta^2 F_z &= \frac{1}{\bar{N}} [\Delta^2 N_{+1} + \Delta^2 N_{-1} + 2N p_1 p_{-1}] \\ &= \frac{1}{\bar{N}} 4N p_1 p_{-1}. \end{aligned} \tag{4.18}$$

The explicit derivation is given in the appendix A.2. This model finally determines the quantum limit set by an N-particle coherent state. Again, we can calculate the fluctuations by inserting the probabilities 4.16 into our model in eq. 4.18 and compare the results to the variance of the observable F_z obtained over all realisations.

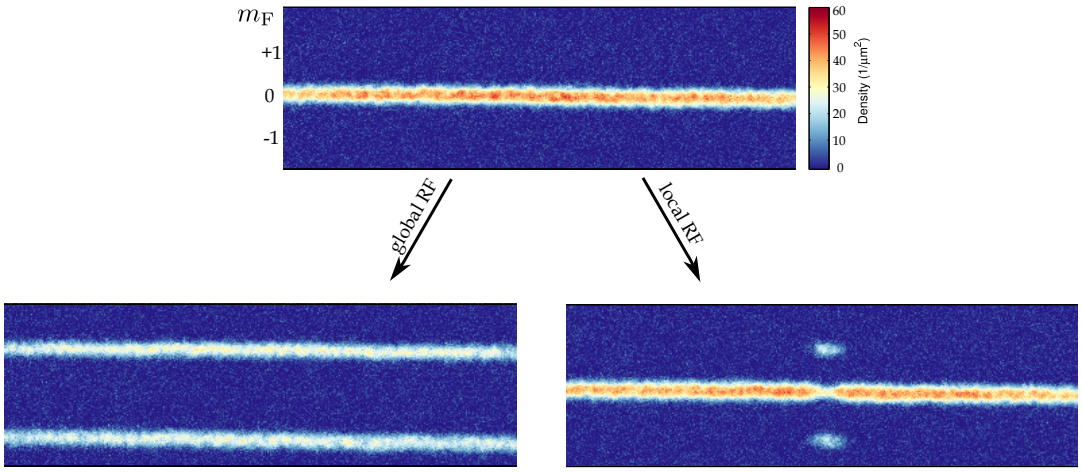

FIGURE 4.7: Starting from the polar state we perform the global spin rotations by applying rf-fields (left) and local rotations using the laser (right). The fluctuations, i.e. variances of the local rotation, are compared to the global cases, which we can prepare very reliably. The local rotation is not performed at $\pi/2$ but in the maxmimum at an angle of $\alpha \approx 50°$.

4.2.4 Experimental Data

Preparing the states

The experimental procedure contains three steps. At first we prepare the atoms in a coherent polar state, i.e. transfer all atoms over an auxiliary state to $|1,-1\rangle \xrightarrow{\pi} |2,-1\rangle \xrightarrow{\pi} |1,0\rangle$. This state represents the polar state in the mean-field phase 2.4 and its fluctuations serve as the technical noise for the next steps to verify that we fundamentally start to a good approximation from the state we expect to prepare. From here we want to apply a global spin rotation, a local rotation at an angle of $\pi/2$ (see fig. 4.7) and calculate for the cases of a global, local or no rotation the fluctuations defined in 4.18. Nevertheless, the local rotation is not performed exactly at $\pi/2$ as anticipated. In fig. A.1, the shot used to calibrate the rotation time for the later used rotations at $60ms$ is shown. There almost the entire population inside the rotation region is transferred to the side-modes. Towards the actual experiment we lowered the imaging power, resulting in a less saturated absorption spectrum. Further, we did not perform the experiment right after this calibration, which could have led to drifts in the rotation power. However, this does not have a qualitative impact on the here discussed results, since the only aim was to compare the fluctuations of one rotation type calculated through the trinomial distribution to its experimentally extracted deviation over all realisations. When starting from $|1,-1\rangle$, the expected F_z value for a local rotation can be described by Rabi cycles of the spin vector rotating around either F_x or F_y periodically in time and is described by $-\cos(x)$-type function. In contrast to this, rotating from $|1,0\rangle$ transfers the atoms symmetrically to the side-modes, hence does not permit to observe the oscillation in the F_z component, but merely in the observable $(N_{+1}+N_{-1})/N_{\text{tot}} = N^+/N_{\text{tot}}$. A $\pi/2$ rotation requires the atoms to be fully transferred to the side-modes, so $N_{+1} = N_{-1} = N/2$, with the ratio to be $N^+/N_{\text{tot}} = 1$. Experimentally, we extract the average of the maximum as $(N^+/N_{\text{tot}})_{\text{exp}} \approx 0.76$ at the peak of the local rotation. From this we can calculate the rotation angle, noticing that the expectation value now possesses a sinusoidal

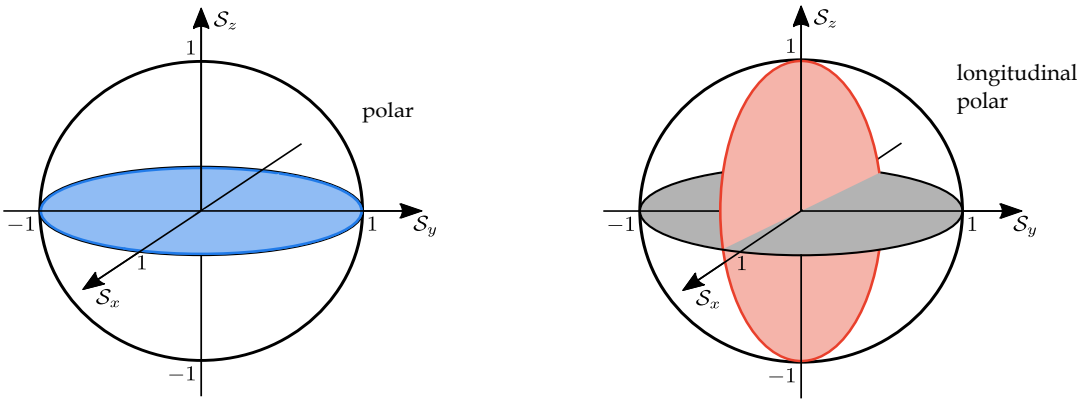

FIGURE 4.8: Polar state (left) and longitudinal polar (right) visualised on the spin sphere together with their respective fluctuations. Both states sit at the centre of the sphere but exert their fluctuations in orthogonal directions. The blue disk spanned in S_x and S_y direction indicates the fluctuations of the polar state. In case of a longitudinal polar state, the red disk representing the fluctuations can be rotated by an angle around the S_z axis. Figures adapted from [21].

functionality (instead of the previously discussed cosine) and can be described at the peak by

$$\langle \frac{N^+}{N_{\text{tot}}} \rangle = \sin(\alpha). \tag{4.19}$$

So the maximal rotation angle we obtain at the peak is $\alpha \approx 50°$. Because of the Gaussian shape of the local rotation in x-direction, we obtain at any other point lower rotation angles. The further implications will be discussed in the context of the results below.

The preparation in $|1,0\rangle$ plays a crucial role. If one would just use the initial level of the condensate, $|1,-1\rangle$, the resulting variance for no spin rotation would be proportional to the total number fluctuations $\Delta^2 F_z \propto \Delta^2 N$, since $F_z = \frac{-N_{-1}}{N} = \frac{-N}{N}$. As a consequence the fluctuations of the initial coherent state could already exceed the cases in which atoms are actually repopulated between the states, which was found to indeed be the case, with the fluctuation of the first being an order of magnitude larger than the latter.

Further, we transfer the atoms to $|1,0\rangle$ via the auxiliary state $|2,-1\rangle$. If the microwave coupling does not transfer all atoms, residual atoms will remain in $|1,-1\rangle$ and $|2,-1\rangle$. We can then use a Stern-Gerlach pulse to clean the atoms out of the magnetically sensitive modes, resulting in a purified condensate.

At this point it is important to notice that adding up the technical (polar state) noise $\sigma^2_{\text{tech}} = \Delta^2 F_z^{\text{pol}}$ and the "theoretical" fluctuation of a state as an estimation for the limit, i.e.

$$\Delta^2 F_{z,\text{limit}} = \sigma^2_{\text{tech}} + \Delta^2 F_z^{i,\text{tri}}, \tag{4.20}$$

with i representing the global/local rotation, is only valid if the mean total atom numbers we use for the normalisation in 4.18 are equal. Since the total atom number fluctuates for the global rotation on the level of $\sim$ 200 atoms ($\sim$ 180 atoms for the local rotation), the presented comparison above between the values is formally not

correct. Instead, we use directly the fluctuations of the total atom number in the polar state, $\Delta^2 N_{\text{tot}}^{\text{pol}}$. Since we compare fluctuations of the quantity $N^- = N_{+1} - N_{-1}$, the polar fluctuations do not depend on the total atom number but merely describe - as mentioned before - the imaging noise. In order to get rid of the noise contribution for local and global rotations, it can be subtracted from the respective number fluctuations before normalising with the total atom number. In that manner, expressions of the form

$$\Delta^2 F_z^j = \frac{\Delta^2 N_j^- - \Delta^2 N_{\text{pol}}^-}{\bar{N}_{\text{tot}}} \tag{4.21}$$

are obtained, with j representing the local or global spin rotation.

Choosing the evaluation regions

The evaluation regions used in the global cases are set equal to the local rotation region for better comparability and the boundaries are estimated manually and capture the points where the local spin rotation seemingly "vanishes". The evaluation radius, i.e. the distance between the averaged centre of the spin rotation to the boundary on one side of the flank is chosen to 15 µm (see fig. 4.9). The atom numbers in a level $|1, m_F\rangle$ are determined by summing all atoms inside the "spin-rotation region" of the respective level.

A comparison between the fluctuations for different evaluation radii for the global rotation is also shown in fig. 4.9. We see that correlations start to build up for smaller evaluation regions with fluctuations even falling below the classical limit, confirming the choice of a 15 µm evaluation radius as a proper choice. The correlations emerge from the absorption imaging of the atoms. The finite width of the point spread function causes the absorption signal to be imaged onto multiple pixels, giving rise to correlations between neighbouring pixels. These correlations are most prominent at the edges of the region and are usually dominated for an increasing evaluation region by the information in between. Further, we observe that the fluctuations increase steadily with larger evaluation regions, hinting towards technical fluctuations. A model to characterise this behaviour can be derived by noting that the imbalance $N^- = N_{+1} - N_{-1}$ possesses information about how far the state is tilted out of the transverse spin plane $S_x S_y$ (fig. 4.9), i.e. the rotation angle. From this we obtain the relation

$$\tan(\theta) = \frac{N^-}{s} \approx \theta, \tag{4.22}$$

where the narrow angle approximation is used. The unnormalised spin length in the plane is $s = N$. Calculating the variance of the left quantity leads to

$$\Delta^2\left(\frac{N^-}{s}\right) = \frac{1}{s^2}\Delta^2 N^- = \Delta^2\theta. \tag{4.23}$$

Rearranging the last equality and transitioning to quantities normalised with the total atom number yields

$$\begin{aligned} \frac{\Delta^2 N^-}{N} &= \frac{s^2\Delta^2\theta + N}{N} \\ &= N\Delta^2\theta + 1, \end{aligned} \tag{4.24}$$

where the manually added term on the right side carries the notion of the shot noise of a coherent state. The first term, linear in N, describes the technical fluctuations because the expression has been normalised to the total atom number and when

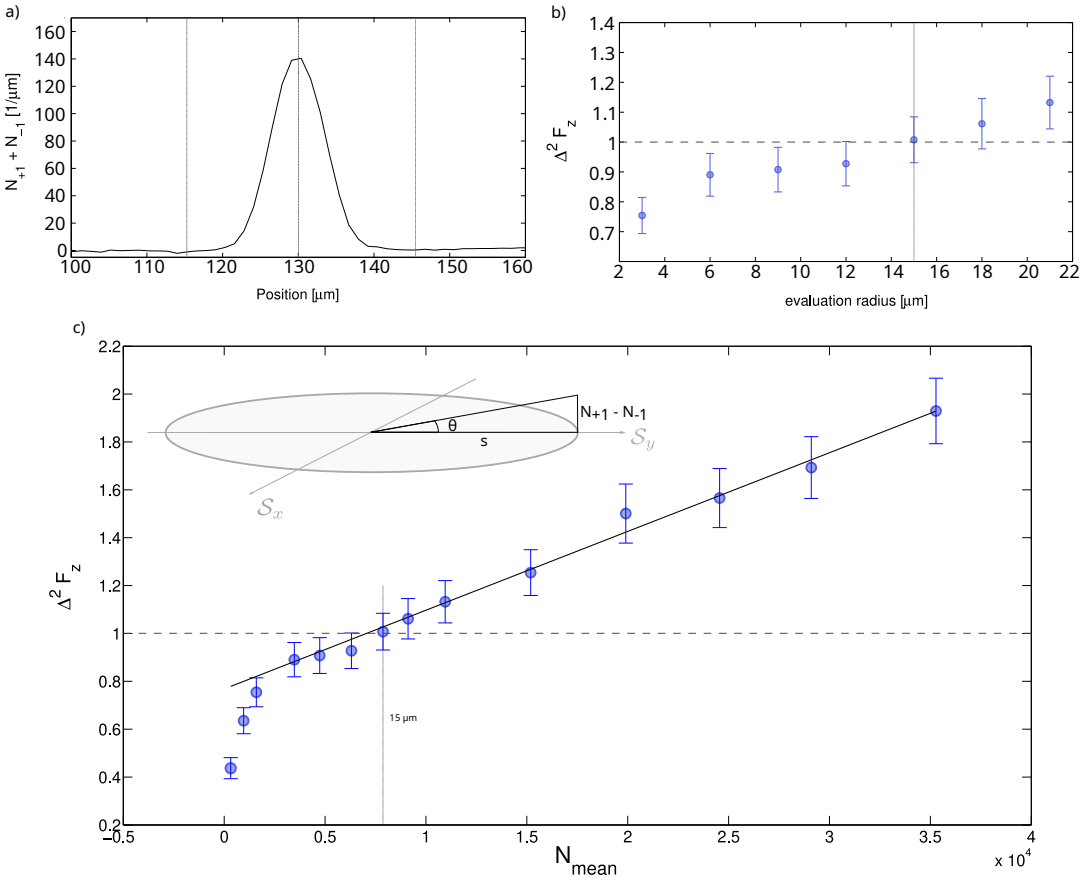

FIGURE 4.9: a) The evaluation region is set according to the local rotation region and is determined by the evaluation radius chosen as the distance between the centre line and one of the dashed lines to 15 µm. There the spin rotation amplitude seems to vanish.
b) The variance of the F_z observable for different evaluation radii is shown. For smaller regions the correlations increase since an atom is imaged on multiple pixels. This effect becomes less dominant the larger the evaluated area is.
c) In contrast to b) the F_z fluctuations are now plotted as a function of the average atom number inside a region of a specific evaluation radius. A linear fit is calculated for radii $> 15\,\mu$m from which the technical fluctuations $\sqrt{(\Delta^2\theta)_{\text{fit}}} = 0.34°$ are obtained as the square root of the slope. The datapoints were sampled from $3 - 21\,\mu$m in $3\,\mu$m steps, from $30 - 70\,\mu$m in $10\,\mu$m steps and additional two points are at $0.5\,\mu$m and $1\,\mu$m.

vanishing, i.e. the rotation angle does not fluctuate ($\Delta^2\theta = 0$), leads to the expected shot noise limit of 1. We can now fit a linear function to the data points and compare the so obtained slope $(\Delta^2\theta)_{\text{fit}}$ and an offset c to the expected values in eq. 4.24. For every setting of a evaluation region a mean total atom number is obtained, which are used as x-values for the fit. Only the values for evaluation regions larger than $15\mu m$, resembling the linear dependency, were used for the fit. In fig. 4.9 it can be seen that the data points indeed lie on a linear function with fit parameters

$$\sqrt{(\Delta^2\theta)_{\text{fit}}} = 6 \times 10^{-3}\text{rad} = 0.34°, \quad c = 0.76.$$

From this we can conclude, that the fluctuations - here now given as the 1 standard deviation - of the global rotation are small, implying that the preparation of the state is highly reproducible. The slope characterises the technical noise above a width of 15 µm, while the behaviour at very small widths, i.e. $1-5$ µm is in good agreement with the model discussed in [21].

Results

The results shown in tab. 4.1 are presented in three steps. In the first row the pure results are given. In the second row a reference picture analysis is included, which is used to remove fringe structures and statistical fluctuations do to the imaging. Detailed information are given in the appendix B. For the third row also the noise removal according to 4.21 is taken into account. The errors on the variances are the statistical estimation of 1 standard deviation (SD) calculated through a jackknife resampling of the data [51]. We used 382 realisations for the case of the polar preparation, 415 realisations for the case of global spin rotation and 434 realisations for the local spin rotations and had on average $\sim 7.5 \times 10^3$ atoms in our evaluation region. For the extraction of the atom numbers, we bin 3 pixels together, because our optical resolution is on the scale of ~ 1.26 µm, meaning that it is not possible for us to clearly resolve structures below this limit.

Preparing the condensate in $|1,0\rangle$ corresponds in the spin-sphere picture to a state which sits in the centre of the sphere and represents the polar state in the mean-field phase diagram 2.4. Its expectation values for the three spin operators vanish, $\langle F_x\rangle = \langle F_y\rangle = \langle F_z\rangle = 0$, with fluctuations only being existent in transverse plane spanned by F_x and F_y as a disk, orthogonal to F_z (see fig. 4.8). The expected fluctuations in z-direction are therefore $\Delta^2 F_z^{\mathrm{pol,tri}} \approx 0$. The results obtained for the F_z-fluctuations including the reference picture analysis, $\Delta^2 F_z^{\mathrm{pol}} = 0.13$, exceed the expected value slightly. The fluctuation level of this polar state represents as discussed before the baseline noise our system contains as technical noise from the preparation and readout procedure. However, we did not consider the photon shot noise. When imaging the atoms, the number of photons used during this process fluctuates for many realisations and transfers an error onto the measured atom numbers. For the extraction of this fluctuation term we can use a noise image and apply a Gaussian error propagation of the measured photon numbers. In previous works conducted on our machine this noise was found to be ~ 0.14 [21], corresponding well to the deviation of the measured fluctuations a polar state entails to the theoretical prediction.
The global spin rotation produces the longitudinal polar state, which sits again in the centre of the spin-sphere but has its fluctuations now along the F_z direction as a disk, with the orientation determined by the Larmor phase (see fig. 4.8). The expected fluctuations of $\Delta^2 F_z^{\mathrm{l.pol,tri}} = 1$ are exceeded by the experimental value on the same scale as before the polar state, $\Delta^2 F_z^{\mathrm{l.pol}} = 1.13$. This validates the necessity to consider the polar state as a fundamental noise level of our system. For the local rotation we obtain a value of $\Delta^2 F_z^{\mathrm{local}} = 0.34$, which at this point is roughly twice as large as the shot noise limit determined for this state, $\Delta^2 F_z^{\mathrm{local,tri}} = 0.16$. The reason as to why the fluctuations of the local rotations are so far below 1 can be explained considering the horizontal rotation profile. Its Gaussian shape and hence flank structure leads to spatially varying rotation angles $\alpha(x)$. The anticipated $\pi/2$ rotation is only achieved at the centre of the rotation region, so only there the state vector is actually rotated into the transverse plane. For this state, the fluctuations in the spin observable F_z

	no rot	global rot	local rot
$\Delta^2 F_{z,\mathrm{exp}}$	0.26 ± 0.02	1.23 ± 0.09	0.45 ± 0.03
$\Delta^2 F_{z,\mathrm{tri}}$	0.002	0.997	0.16
$\Delta^2 F_{z,\mathrm{exp}}$	0.13 ± 0.01	1.13 ± 0.08	0.34 ± 0.02
$\Delta^2 F_{z,\mathrm{tri}}$	-0.004	1	0.16
$\Delta^2 F_{z,\mathrm{exp}}$	-	1.0 ± 0.08	0.21 ± 0.02
$\Delta^2 F^s_{z,\mathrm{tri}}$	-0.004	1	0.16

TABLE 4.1: The first block does not contain any correction, the second block includes the reference picture analysis, and the third block includes the reference picture analysis and noise removal from the polar state. The average atom number is $\sim 7.5 \times 10^3$ inside an evaluation region of 30 µm. The maximum local rotation angle is $\alpha \approx 50°$. For the trinomial values of the polar state slight deviations from 0 are obtained in both directions. This occurs most likely due to noise from our optical system, such as thermal fluctuations and vibrations, which might contribute negative numbers to the empty levels $m_{F=\pm1}$ and hence to the probabilities $p_{\pm1}$

are maximal. Moving away from the centre, the rotated states do not experience the full $\pi/2$ rotation. The resulting state, if represented in fig. 4.8, would be tilted between the polar and longitudinal polar state. Here, additional fluctuations arise in the transverse components simultaneous to a reduction of the projected fluctuations on F_z below 1. A summation of all atoms inside an evaluation region leads then to an average rotation angle, therefore yielding an overall fluctuation level of $\Delta^2 F_z < 1$.

Removing the imaging noise by using eq. 4.21 with $\Delta^2 N^-_{\mathrm{pol}} \sim 960$ reduces the experimental fluctuations of the longitudinal polar state, i.e. the global rotation to the expected value $\Delta^2 F_z^{\mathrm{l.pol}} = 1.00 \pm 0.08$. For the local rotation we obtain 0.21 ± 0.02, which still deviates $\sim 15\%$ from the classical limit. This hints towards further contributions to the preparation noise. Comparing this to the results obtained in [47] shows that we managed to reduce the fluctuations by an order of magnitude. The results are presented in tab. 4.1, where the results without the previously discussed noise removal are presented together with the results after the optimal reference picture analysis and additionally after subtracting the imaging noise.

One last remark concerns the fluctuations for the polar state calculated with the trinomial distribution in eq. 4.18. For the calculation, the particle numbers in the empty side modes are needed for the probabilities $p_{\pm1} = N_{\pm1}/N$. Here, fluctuations of the imaging system, such as the laser, thermal noise on the camera, vibrations of the imaging optics can contribute also "negative" atom numbers, leading to negative probabilities and ultimately negative fluctuations.

Chapter 5.

Soliton Formation Analysis

Recent works conducted on three-component vector solitons in BECs were primarily concerned with the description of the macroscopic properties, such as their velocity, width, darkness and spatial structure of the phase. However, the dynamics of the internal spin states were analysed so far by observation of the collision between two pairs of solitons [17]. Both cases require that the solitons are already generated in the condensate. But using the local spin rotations our experiment provides, we first generate local perturbations, partially transferring atoms from $|1,0\rangle$ to $|1,\pm1\rangle$, out of which after a certain time evolution period the solitons emerge. In this chapter we experimentally investigate the internal dynamics of the solitons during their formation process. To motivate this further, one could think e.g. of the $|1,\pm1\rangle$-levels after the initial density perturbation as a potential in which the atoms sit, allowing them to interact. While the separation proceeds, a double well potential starts to form with a dynamically increasing barrier. During this time, the atoms are assumed to still be able to interact and to jump between the two potentials, a process known as tunnelling. After the separation is completed, the two bright components of separate three-component vector solitons emerge. In that state the barrier between the two potentials reaches its maximum, i.e. the interaction between the separate objects ideally ceases to exist and the individual internal states are fixed. Consequently, the spin observables of initially interacting quantum systems and their evolution during the soliton formation are an promising frame for the search of e.g. EPR-correlations similar to [52] or squeezing properties. The latter is a process in which the fluctuations of one variable reduces below the level postulated by the Heisenberg limit, at the cost of an increasing fluctuation of the conjugate variable. So in order to investigate this types of correlations in scenarios like colliding solitons, it is crucial to guarantee a preparation and control of the solitons on coherent state level.

5.1 Generating solitons

An extensive discussion of the experimental realisation of solitons and imprint of the necessary phase as well as the extraction of the density profiles in our system can be found in [16]. This section discusses briefly some prominent features in the density profiles during the separation.

The Rabi frequency profile along the condensate (x-direction) for each beam is described by a Gaussian $\Omega(x) = \Omega_0 exp(-x^2/(2\sigma^2))$. The beam width determines the radius $\sigma = w/2 = 3.5\,\mu m$. Conceptionally, for the entire amplitude exerted by the successive beams, we first have to extend this picture to 2 dimensions and calculate then the time integral $\int \Omega(x,y)dt$. Every time step is linked to a discrete y-value $\{y_1,..,y_6\}$ for each pulse in y-direction, where the overlap of the beams must be

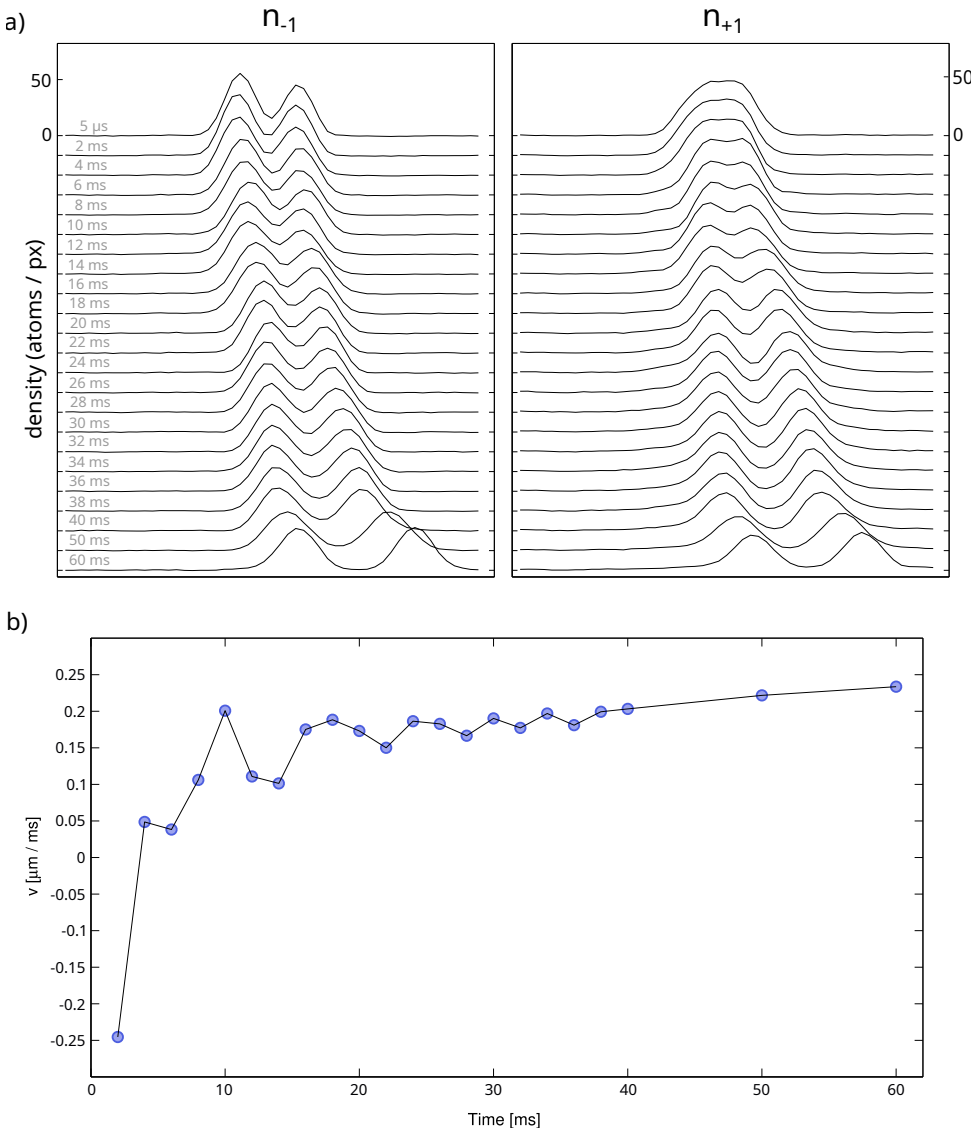

FIGURE 5.1: a) Time evolution of the density profiles in the side-modes after an initial local rotation with the total rotation time $\tau = 95\,\mu s$ resulting in two solitons propagating in opposite directions. The static term of the fictitious magnetic field pointing along the laser direction resembles a potential for the atoms which acts attractive for $|1, +1\rangle$ and repulsive for $|1, -1\rangle$ hence leading to a clumping or rather separation of the density structures at early times. A background motion of the condensate additionally shifts the centres of the separating regions to the right.
b) The drift velocities are determined considering the centre between two peaks in an averaged profile for a certain time and their distance to the initial rotation position. Starting with motion to the left (negative velocities) the condensate sloshes to the right side (positive velocities).

considered. In addition, the transfer of the atoms also depends on the pulse duration τ, altogether allowing us to express the transfer fraction as $(n_{+1} + n_{-1})/n_0 = \sin(\Omega(x)\tau)$. However, the choice of the appropriate pulse duration is not entirely clear-cut, since we obtain solitons in a range of $\sim 20\,\mu s$. There is just a small frame though in which the resulting objects do not show any blurry features around the bright components, which indicate a shedding of atoms. From this observation, we used a Rabi pulse of $\tau = 95\,\mu s$, separated over the 6 pulses in our previously discussed rotation scheme. The soliton formation is finished at $\sim 60\,ms$. In fig. 5.1 the density profiles n_{+1} and n_{-1} during the separation are shown. As discussed in [16], the time-scales on which we would observe the excitations to be dispersive is on the scale of the separation process. So by seeing the non-dispersive behaviour, i.e. formation of two stable peaks, and ensuring that the blurry features are reduced, we conclude, that we indeed prepared solitons. The density profiles show a distinct difference. For early times after the local spin rotations, the atoms in $m_F = -1$ are already getting separated in contrast to $m_F = 1$. This feature occurs due to the static term of the fictitious magnetic field B_0^{fict} exerted by the local control laser, as introduced in sec. 3.2.4. Since this field is oriented parallel to the laser it adds vectorially to the magnetic offset field, resulting in a slight tilt of the quantisation axis. Another consequence is that this magnetic field acts as a potential to the $m_F = \pm 1$ components. Since the magnetic field is oriented in transversal direction, a gradient acts in longitudinal direction along the condensate. The resulting potential is repulsive for $m_F = -1$ and attractive for $m_F = +1$ [16].

Another feature is that while the initial density perturbation is separating, there is an additional motion to the right. This can be linked to a relative motion of the background condensate to the local perturbation. Loading the condensate into the WG can cause it to slosh back and forth, something that can be avoided by a slower ramp of the XDT and WG lasers. The velocity of this sloshing adds then vectorially to the solitons motion. This background motion can be estimated using the centre-of-mass and to do so, we effectively calculate $v_c(t) = (x_c(t) - x_c(0))/t$, where $x_c(t)$ is the centre between the separating peaks at a time t and $x_c(0)$ the initial position of the local spin rotation. For the estimation of the centre we use the profiles averaged over all realisations for one time and fit a double gaussian function to extract the positions of the two amplitudes. Using this procedure, we obtain the velocities presented in fig. 5.1. Here, we see that an initial motion to the left at 2 ms is followed by an acceleration in the opposite direction. The results should be taken with caution though. Estimating the background velocity in this way is a rough estimation and depends strongly on the extracted centres, hence on the positional information of the peaks. Prevalent asymmetries in the separation or background condensate are not taken into account.

As mentioned in 2.4, we do not apply microwave dressing of the system, which essentially sets the quadratic Zeemen shift q at a high value. In doing so, the spin-changing collisions are expected to be far off-resonant and to not affect our system.

5.2 Soliton Splitting dynamics

This section presents the time evolution of the atom numbers and spin observables of the different modes before the solitons have emerged. As introduced earlier, the exchange of atoms between the continuously separating peaks is assumed to be high shortly after the local rotation was performed and to decrease in time, resulting in a

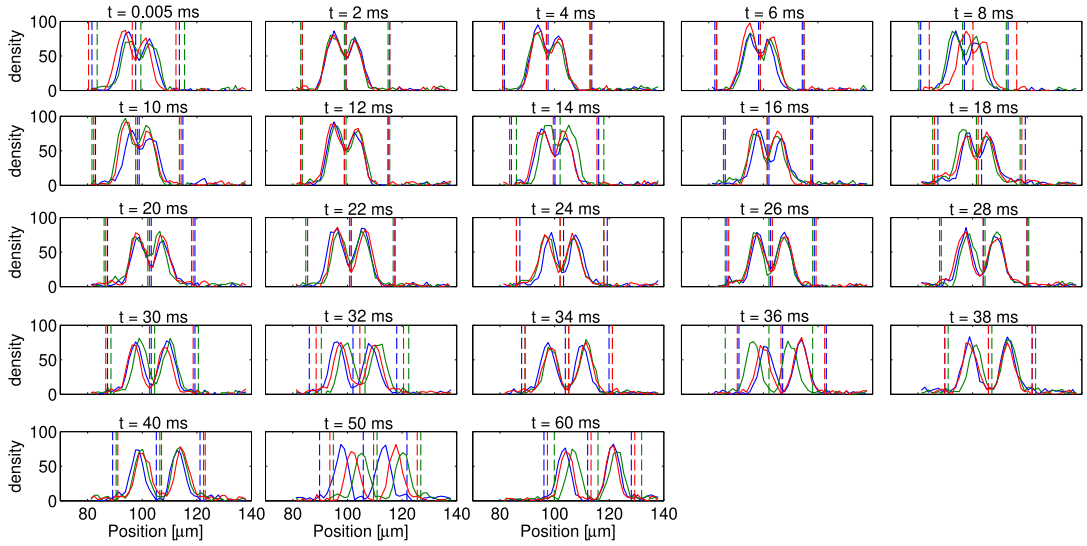

FIGURE 5.2: Three randomly picked realisations for each time are shown including the individual evaluation regions used for the extraction of the atoms on the left and right side. To ensure the signal can be evaluated properly, we used the combined density profile $N_{+1} + N_{-1}$ to determine the centre and the outer boundaries at a distance of 16 µm relative to it.

fixed configuration once the solitons emerged. In our experiment we measured the evolution of the soliton in 2 ms steps up to a total time of 60 ms, where the soliton formation was finished.

Further we also investigate the evolution of the F_z observable by taking the difference $F_z^{\mathrm{l}} - F_z^{\mathrm{r}}$ (see sec. 5.2.2).

5.2.1 Setting the evaluation regions

To access the populations and consequentially spin observables, we first have to define spatial regions of interest. This includes the boundaries at the sides of the rotation region, where the rotation amplitude seemingly vanishes, and a point characterising the separation between the two peaks. We use the sum of both side modes $N_{+1} + N_{-1}$ to obtain a better signal-to-noise ratio. The sum of both levels also resembles the spatial structure of the $|1, -1\rangle$ mode, allowing for a more precise extraction of each density peak and ultimately the evaluation regions. The centre between the two peaks is determined individually for each realisation, because of horizontal positional fluctuations of our local rotation setup. As a consequence, atoms might be added to the wrong side in the evaluation, affecting the atom number dependent observables. The horizontal fluctuations occur on the scale $\sim$ 8 µm, on which the Thomas-Fermi density profile of the condensate does not vary considerably. The left and right boundary are then set to a fixed range of 16 µm from the centre. The chosen evaluation regions for each time are shown in fig. 5.2. The atom numbers on the left side are extracted similar to 4.2.4 by summing the atoms from the left boundary to the centre and accordingly from the centre to the right boundary, giving us arrays of numbers for every side and magnetic state

$$N_{+1}^{\mathrm{l}}, N_{+1}^{\mathrm{r}}, N_{-1}^{\mathrm{l}}, N_{-1}^{\mathrm{r}}. \tag{5.1}$$

Additionally, we calculate the sum of each side as

$$N^{\mathrm{l,r}} = N_{+1}^{\mathrm{l,r}} + N_{-1}^{\mathrm{l,r}}. \tag{5.2}$$

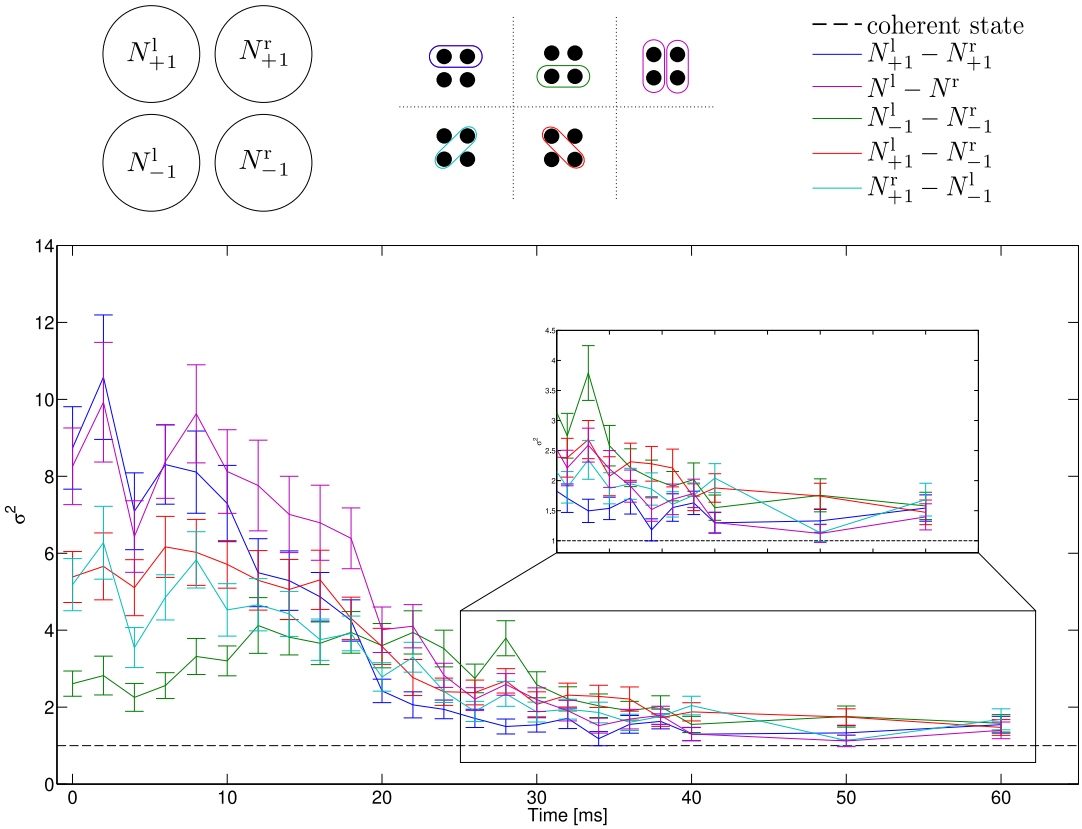

FIGURE 5.3: The variances of different types of differences between atoms on the left (l), right (r) and in $m_F = +1$ or $m_F = -1$ are shown in the lower figure as a function of the evolution time. The upper figure shows schematically the "blops" we use to calculate the respective difference and is colour-coded accordingly. We see that the variance lowers with increasing time and approaches for evolution times > 25 ms the classical limit set by a coherent state. However, the fluctuations always remain above the limit and reach the lowest fluctuations, $\sigma^2 = 1.40 \pm 0.22$, for $N^{\mathrm{l}} - N^{\mathrm{r}}$.

5.2.2 Combined variables of different modes

For the evaluation we consider different combined variables, similar to the notion of EPR variables, as sketched in fig. 5.3 in the upper row. There, the different coloured areas denote the components of our pre-soliton that are subtracted, such as e.g. $N^{\mathrm{l}}_{+1} - N^{\mathrm{r}}_{+1}$ in the simple case or crossed combinations like $N^{\mathrm{l}}_{-1} - N^{\mathrm{r}}_{+1}$. In that manner we analyse all different combinations between the left and right side. The subscript denotes the magnetic level m_F and the superscript if we consider the left (l) or right (r) peak. To motivate this approach further as why to consider in particular the difference of the atom numbers, we can think of it in the following way. The total atom number is fixed for one realisation. During the separation we assume the difference to fluctuate due to tunnelling processes. If the process of distributing atoms over the two sides is repeated M times, then a high fluctuation level would correspond to a random distribution of the atoms, i.e. they are not distributed in a preferred way. With ongoing separation the interaction is then expected to resemble more and more the situation of two independent objects.

	$N^{\mathrm{l}}_{+1} - N^{\mathrm{r}}_{+1}$	$N^{\mathrm{l}} - N^{\mathrm{r}}$	$N^{\mathrm{l}}_{-1} - N^{\mathrm{r}}_{-1}$	$N^{\mathrm{l}}_{+1} - N^{\mathrm{r}}_{-1}$	$N^{\mathrm{r}}_{+1} - N^{\mathrm{l}}_{-1}$
σ^2	1.54 ± 0.22	1.40 ± 0.22	1.58 ± 0.23	1.47 ± 0.21	1.68 ± 0.27

TABLE 5.1: The fluctuation of all types of atom number differences after full separation of the solitons at 60 ms exceed the coherent state level $\sigma^2_{\mathrm{coh}} = 1$. Even after considering the errors an excess fluctuation of $\sim 20 - 30\%$ is present. This hints towards additional fluctuations, which can not only occur during the preparation but also during the separation process. One can note that the particle number difference of the separated solitons should resemble the situation of a coherent state, i.e. the solitons are independent objects. Here no separation has been inserted yet to account for classical correlations. But up to a separation of 10.08 µm the fluctuations remain in good agreement.

The fundamental fluctuation level is once again set by the coherent state. If the separation of the initial density peak is at all times described by a coherent state, we can assume the total fluctuations of the system to be comprised by two independent coherent states. In contrast to eq. 4.18, where we determined the fluctuations of the combined variable comprising the atom number difference between the side-modes $N_{+1} - N_{-1}$, we now consider the number difference between the left and right side, e.g.

$$N^{-} = N_{\mathrm{l}} - N_{\mathrm{r}}. \tag{5.3}$$

Inserting this into the results obtained in A.1 we obtain as the coherent state level, normalised to the total atom number,

$$\Delta^2 N^{-} = 1. \tag{5.4}$$

For the experimental data we use the F_z readout, providing us with the spatial separation of the initial local rotation over time. The fluctuation of each time is normalised by the corresponding average total atom number $\langle N \rangle$ of the evaluated modes calculated from samples of ~ 105 realisations. Since we manually post process the data to filter out unusable shots, the number of realisations varies for the different times slightly. A jackknife resampling of the data was used again to calculate the errors on the variances as 1 standard deviation. The results are then compared to the limit set by 5.4 and shown in fig. 5.3. It can be seen that initially the fluctuations are very high. But with ongoing separation the variance in the atom number difference and their respective errors decrease for all different combinations. The most prominent reduction, can be found in the difference $N^{\mathrm{l}}_{+1} - N^{\mathrm{r}}_{+1}$ (blue line), which has the most significant drop of the fluctuation over time and ends up at $\sigma^2 = 1.54 \pm 0.22$ after 60 ms. The lowest value is obtained for the difference $N^{\mathrm{l}} - N^{\mathrm{r}}$, which reaches $\sigma^2 = 1.40 \pm 0.22$ after the separation completed. At high times the fluctuations of the various types of differences reach similar results within their respective errors (see tab. 5.1). However, all fluctuations remain above the classical limit and deviate by roughly $20 - 30\%$ from this coherent state level. This hints towards additional fluctuations influencing our state preparation. Another contribution to the fluctuations can be due to the sloshing of the condensate. This essentially leads to a soliton propagating in the same direction as the condensate and one propagating in the opposite direction. The width and atom numbers of a soliton are restricted together with the velocity by the chemical potential as given in eq. 2.30. The accelerating background clearly effects the velocity of the solitons asymmetrically and it is not clear how this

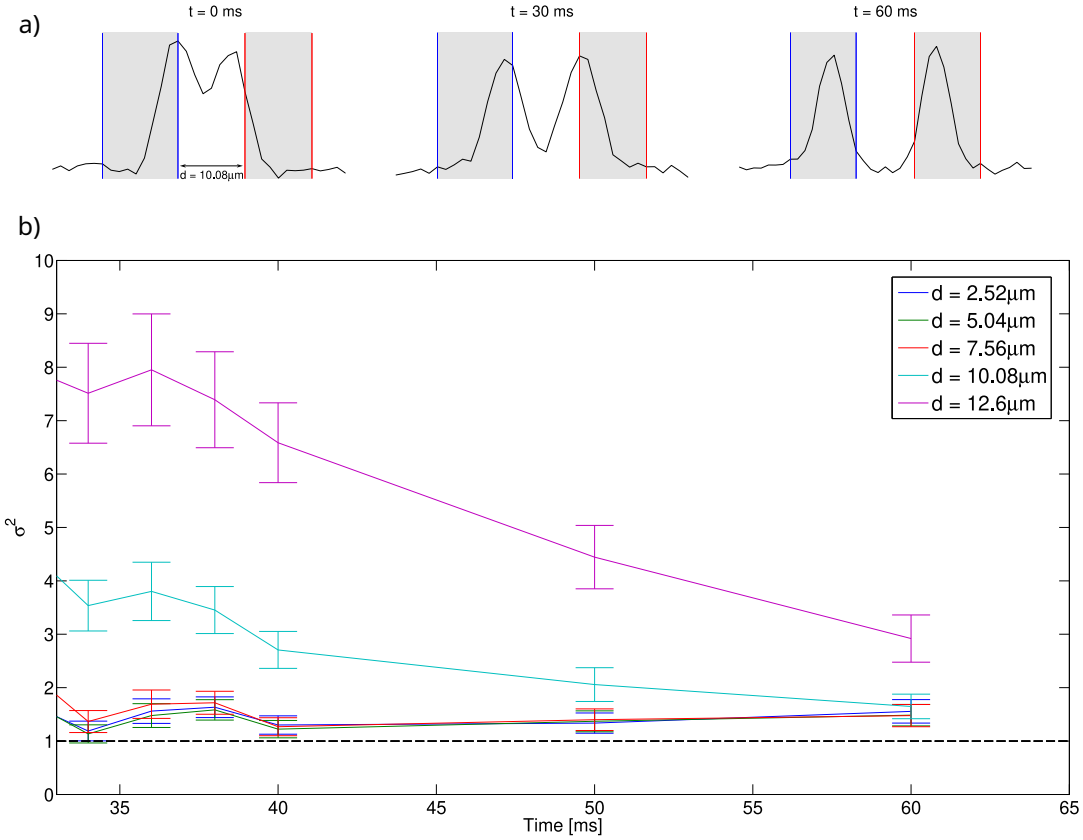

FIGURE 5.4: a) The evaluation regions shown as grey ares confined by the boundaries for the left (right) side coloured blue (red) are separated by a distance of 10.08 µm, here shown for three stages of the separation, after the local rotation, after 30 ms and after 60 ms. For the analysis, the atoms contained inside the grey areas are summed for each side. For early times, the entire extension of the density perturbation is ~ 18 µm. So, separating the evaluation regions ejects the majority of the atoms in the sides. With ongoing propagation a sufficient separation while maintaining the atom number information can be achieved.
b) The fluctuation of the combined observable $N^- = N^l_{+1} - N^r_{+1}$ is shown for distances separating the two sides. As explained in a) we only consider the later times, for which we observe a good agreement of the fluctuations up to a separation of 12.6 µm. At this separation, even after 60 ms and full separation of the initial perturbation the inner boundaries start to cut into the peaks, hence leading to an ejection of the atoms.

translates into the populations inside the peaks. Studying the macroscopic properties could give more insight into this process. Preferably the sloshing and other trap dynamics are eliminated to reduce possible effects and allow for a symmetric preparation. It must be also noted that an optimal reference picture analysis was applied again to reduce the fluctuations and remove possible fringes on the images. Nevertheless, it can be concluded that after the separation completed, the two solitons act indeed as independent objects and exert their interaction only during the separation phase. In this period the observed high fluctuations are linked to the exchange of particles between the sides.

In [53] it was found that when evaluating correlations between two adjacent evaluation regions a separation must be introduced to account for e.g. the atoms simultaneously imaged on both sides, thus creating classical correlations. However, choosing reasonable separation distances for our measurements proves to be hard for the early times, since we reduce an already narrow gap in which we count atoms further, adding an increasingly higher contribution of the area containing noise (see fig. 5.4). Another problem occurring at early times is that we define the two evaluation regions according to the centre between the two peaks. An imprecise estimation of the individual positions of the peaks, hence the centre between them can cause the evaluation regions to be cut in an unfavourable way, where one side includes more atoms of the peak than the other. This problem reduces though with ongoing propagation time due to the progressing separation. But since the fluctuations are far above the coherent state level at early times anyway, it allows us to focus the analysis on the later times $t > 30\,\mathrm{ms}$. It must be also noted that the boundaries have been determined using the combined atom numbers $N_{-1} + N_{+1}$ and the separation then introduced on top of these results. But due to the local rotation laser, the side-modes underlie a different systematic, where the atoms in $m_F = +1$ experience an attractive potential, so bunch up, while the atoms in $m_F = -1$ a repulsive potential and already show a separation of the peak. This has not been taken into account here, but can add a systematic error to the results, because at early times more atoms can be discarded out of the $m_F = -1$ level, due to the already prevalent separation. At late times the peaks are separated in both modes and this effect should not impact the results strongly. In fig. 5.4 the fluctuations of the previously discussed observable $N^{\mathrm{l}}_{+1} - N^{\mathrm{r}}_{+1}$ is shown for the different separation distances. It can be seen that with an increasing separation until $d = 10.08\,\mu\mathrm{m}$ the fluctuations reduce to a similar level within the error bars at later times. Moving towards bigger separations, i.e. $d > 10.08\,\mu\mathrm{m}$ adds noise to our data where the fluctuations for the latest times begin to exceed the coherent state level strongly. It is this separation limit after which the inner boundaries of both evaluation regions start to cut prominently into the density peaks even at 60 ms, resulting in the same problems as before at early times.

A few words must be added to the chosen separation distances displayed in fig. 5.4. We obtain the measured densities in the form of matrices, of which the rows denote the respective shot and the columns the density information per binned pixel. As mentioned earlier, we bin three pixels together to analyse the information on a scale corresponding to the resolution of our system of $\sim 1.26\,\mu\mathrm{m}$. As a consequence, the positional information is discrete, making it particularly hard to set a specific spacing. Rather than setting a fixed distance in μm, the distance is determined in units of bins, i.e. 1-5 bins symmetrically in both directions around the centre. So for a shift of the boundaries of 4 bins to the left and right, the total distance is fixed at 8 bins and taking into account the size of each bin $s_{\mathrm{bin}} \approx 1.26\,\mu\mathrm{m}$, this results to $d = 10.08\,\mu\mathrm{m}$.

5.2.3 Evaluation of F_z

The atom numbers extracted for each excitation on both sides can be used to calculate the F_z spin of each side respectively using equations 3.14. The variances are calculated considering all realisations for a respective spin observable and its error is once again determined as the 1 standard deviation via a jackknife resampling. The results for the F_z-measurement is shown in fig. 5.5. Here we considered the combined variable

$$F_z^{\pm} = F_z^{\mathrm{l}} \pm F_z^{\mathrm{r}}, \tag{5.5}$$

between the left and right side. Similar to sec. 5.2.2, this represents again EPR-type variables. We use the same procedure as introduced in sec. 4.2.3 to estimate a fluctuation limit. So calculating the limit for the difference in the F_z spin between two sides would demand an expression like

$$\begin{aligned} \Delta^2 F_z^{\pm} &= \langle (F_z^{\pm})^2 \rangle - \langle F_z^{\pm} \rangle^2 \\ &= ... \\ &= \Delta^2 F_z^{\mathrm{l}} + \Delta^2 F_z^{\mathrm{r}} - 2(\langle F_z^{\mathrm{l}} F_z^{\mathrm{r}} \rangle - \langle F_z^{\mathrm{l}} \rangle \langle F_z^{\mathrm{r}} \rangle). \end{aligned} \tag{5.6}$$

Evaluating the covariance between the two observables, i.e. the third term is in so far complicated that we need knowledge about the specific state we are investigating. The required eigenstate $|\psi\rangle$ for the expectation value $\langle F_z^{\mathrm{l}} F_z^{\mathrm{r}} \rangle$ is now defined on an extended Hilbert space $\mathcal{H} = \mathcal{H}_{\mathrm{l}} \otimes \mathcal{H}_{\mathrm{r}}$ and is generally not separable. Further, the last two terms can be understood as a measure of correlations inside our system. For highly correlated states, $\langle F_z^{\mathrm{l}} F_z^{\mathrm{r}} \rangle$ is dominating, hence reducing the overall fluctuations, while for an uncorrelated state this term is separable. So, considering the preparation of two separate non-interacting objects, i.e. coherent states that fluctuate independently, the expectation value of two observables decomposes to a product of expectation values like

$$\langle F_z^{\mathrm{l}} F_z^{\mathrm{r}} \rangle = \langle F_z^{\mathrm{l}} \rangle \langle F_z^{\mathrm{r}} \rangle. \tag{5.7}$$

Inserting this back into eq. 5.6 reduces the expression for the variance to the sum of the individual fluctuations,

$$\Delta^2 F_z^{\pm} = \Delta^2 F_z^{\mathrm{l}} + \Delta^2 F_z^{\mathrm{r}}, \tag{5.8}$$

where the fluctuation of each F_z is determined by the probabilities of populating the respective levels. The individual fluctuations are calculated for each side via A.9. For the normalisation, the average atom number of the analysed system was chosen. To be in accordance with the theoretical approach, we considered values of the form

$$F_{z,\mathrm{exp}}^{\pm} = \frac{(N_{+1}^{\mathrm{l}} - N_{-1}^{\mathrm{l}}) \pm (N_{+1}^{\mathrm{r}} - N_{-1}^{\mathrm{r}})}{\bar{N}} \tag{5.9}$$

The comparison of the experimental data to this limit set by two non-interacting coherent states is presented in fig. 5.5, where the ratio between the experimental and trinomial values are given for each time. In addition to the combined observables, the results for the individual sides are also shown. It can be seen that for the combined observables $F_z^{\mathrm{l}} \pm F_z^{\mathrm{r}}$ even when the evaluation regions are separated by $10.08 \mu m$ the fluctuations reduce to the expected coherent state level within the errorbars. The results for 60 ms are given in tab. 5.2. There it is shown that for smaller separations the experimentally obtained values together with their errors lie below the "theoretical" values.

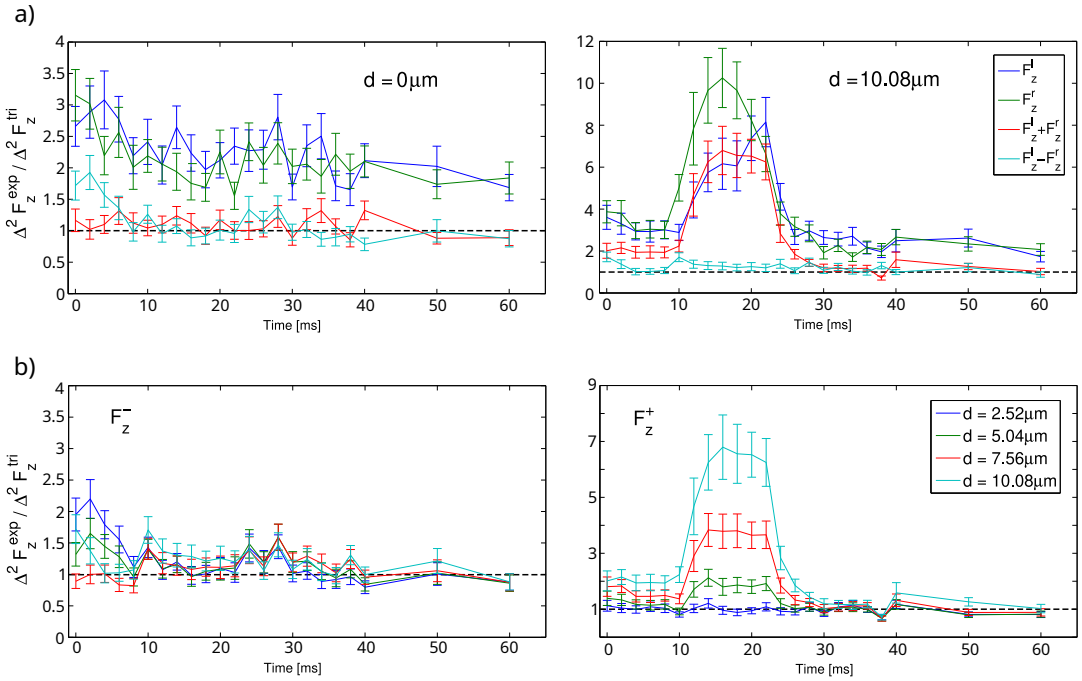

FIGURE 5.5: a) The time evolution of the F_z variance for the separate sides and combined variables $F_z^{\pm}$ are shown. On the left both evaluation regions are not separated, while on the right side the maximum still applicable separation as discussed in sec. 5.2.2 is used. The fluctuations of the combined variables drop in both cases to the classical limit at late times.
b) The variance of the combined variables is shown for different separation distances. For F_z^-, the evolution is very similar for the different separations. The analysis of F_z^+ reveals a sharp rise and decrease for 10-28 ms. This plateau increases with larger separation and is explained in the main text.

As discussed previously, introducing a separation of the regions at earlier times neglects a significant fraction of the atoms inside the peaks, leading to a loss of information. However, it can be seen, that an increasing separation has different effects on the sum and difference between the F_z components. While it does not strongly effect the fluctuations of the difference $\Delta^2 F_z^-$, a sharp rise and decrease between 10 and 28 ms can be observed for the sum and individual components, i.e. $\Delta^2 F_z^+$ and $\Delta^2 F_z^{l,r}$. A possible explanation is that the evaluation regions cut out large parts of the actual peak at early times. With progressing separation, the majority of the peaks get shifted into the evaluation regions and the expected signal emerges as higher fluctuations. These lower then with ongoing time to the coherent state level of two independent objects.

Overall, this shows the reliable production of solitons with fluctuations in the combined observables on coherent state level. This result enables us to consider the combined observables $F_z^{\pm}$ as proper candidates for the investigation of e.g. spin squeezing in processes like soliton collisions. Generally, it is most promising to look for proper conjugate variables in combined observables of the transverse spin components $F_{x,y}$. As discussed in 5.1, in deriving the Manakov model for vector solitons the quadratic Zeeman shift is neglected by setting $q = 0$. Experimentally, this is achieved by not applying microwave dressing, essentially giving us a high value

	2.52 µm	5.04 µm	7.56 µm	10.08 µm
r^+	0.81 ± 0.11	0.82 ± 0.11	0.89 ± 0.13	1.02 ± 0.15
r^-	0.88 ± 0.13	0.86 ± 0.13	0.87 ± 0.14	0.88 ± 0.13

TABLE 5.2: The relative variance $r^{+,-} = \Delta^2 F_z^{\mathrm{exp},(+,-)} / \Delta^2 F_z^{\mathrm{tri}}$ for different separation distances after full separation at 60 ms. Without separation of the adjacent evaluation regions, classical correlations occur at the boundary due to the simultaneous imaging of an atom in both regions. For separations below 10.08 µm the fluctuations of F_z^+ are found to be slightly smaller than the corresponding value calculated with the trinomial distribution 5.8. Even when considering the errorbars they still fall below the theoretical value. At a separation of 10.08 µm the fluctuations correspond to the classical limit. The fluctuations of F_z^- correspond within the errorbars to this classical limit.

of q. As a consequence, the possible rotations are restricted to the spin-sphere, because it is the quadratic shift which, by changing the spinor phase, allows to rotate the state on the so-called spin nematic sphere onto a quadrupole. By preventing this rotation we justify the previously made assumption to focus the analysis to a SU(2)-subspace containing solely the generators $\{F_x, F_y, F_z\}$. To pursue this question further, a scheme is needed which provides a readout of not only the F_z spin but simultaneously the transverse components $F_{x,y}$.

Chapter 6.

Conclusion and Outlook

This work presented the implementation of a local rotation pulse scheme, which aimed to compensate the relative motion of the condensate and laser in order to reduce the vertical positional fluctuations, thereby increasing the stability of the local rotation setup. By solving this, we wanted to ensure a local spin rotation with a stable rotation amplitude and reduced fluctuations of the spin observables on the order of the coherent state limit. To do so, the AOD responsible for the vertical deflection of the laser was pulsed to generate 6 partially overlapping Gaussian beams, resembling a plateau-like intensity profile, where the Gaussian flanks do not coincide with the condensate. The measure we used to trace the success of this implementation was the F_z observable, since it is easily accessible.

We showed that we can not only broaden the effective beam on the atom cloud but also reach a flat rotation profile. This ensures that the rotation amplitude exerted on the atoms is "constant" over an extended spatial region. We were also able to eliminate the spike structure in the rotation spectrum by implementing a buffer time of $t_{\text{off}} = 6.5\,\mu\text{s}$. During the overlap between the laser entering the AOD and two different frequencies in the AOD crystal, the beam can get deflected simultaneously in two directions and interfere. The buffer time ensures, that the laser gets only deflected by one acoustic wave at a time.

We then determined the stability of the rotation amplitude when performing $\pi/2$ local spin rotations out of the $|1,-1\rangle$ level. Here different central frequencies were used to shift the 6 pulses over the condensate. The rotation angle fluctuations over this extended frequency range of $\sim 0.3\,\text{MHz}$ are $\sqrt{\Delta^2\alpha} = (5.62 \pm 0.84)^\circ$. Compared to the extension of the coherent state of $\sim 6.2^\circ$ this leads to an increase of the expected state on the spin sphere to almost twice the size in the F_z direction.

In the next step we focused on $\pi/2$ rotations starting with the $|1,0\rangle$ level. The rotation scheme was tested by comparing the F_z-results to the quantum limit set by a coherent state. To this end, three states were prepared, namely the polar state (no rotation), the longitudinal polar state (global rotation) and the local rotation and compared their fluctuations of F_z with the values determined from a statistical model. It was shown, that the local rotation was performed in the maximum at $\alpha = 50^\circ$ due to an experimental error, but had otherwise no influence on the results, since the F_z-fluctuation can still be compared to the statistical value. To reduce further statistical noise from the imaging process and remove fringe structures on our images a reference picture analysis was implemented. While the results for the polar and longitudinal polar states are consistent with the expected values, it is shown that the fluctuations of the local rotations deviates by $\sim 15\%$ from its model. This points towards additional fluctuation sources which were not considered in this thesis but will be discussed briefly below.

In the last step we used the local rotation scheme to generate solitons and measured the formation process up to the time were the solitons fully emerged at 60 ms.

We analysed the evolution of the atom number distribution over the different "sides" and considered combined variables of the atom numbers $N_{\pm 1}^{\mathrm{l,r}}$ and $F_z^{\mathrm{l,r}}$, of which we analysed again the fluctuations. We found that with progressing time the fluctuations of $F_z^{\pm} = F_z^{\mathrm{l}} \pm F_z^{\mathrm{r}}$ reduce from an initially high level to the level expected for a coherent state and falls at the point of full separation even slightly below. The lowest values as ratios of the experimental result and theoretical expectation $r^{\pm}$ are $r^{+} = 0.81 \pm 0.11$ and $r^{-} = 0.86 \pm 0.13$. However, the fluctuations of the combined variables comprised of the atom numbers had its strongest reduction for the observable $N^{\mathrm{l}} - N^{\mathrm{r}}$. The obtained value after full separation is $\sigma^2 = 1.40 \pm 0.22$. Considering the errors, deviations from the classical limit $\sigma^2_{\mathrm{coh}} = 1$ in the range of $\sim 20 - 40\%$ were obtained. An explanation for this may be found in the asymmetry of the preparation, resulting from a sloshing and therefore accelerating background. While one soliton moves with the background, the other walks against the background motion, impacting the velocities and hence possibly influencing the atom numbers inside the solitons, leading to increased fluctuations. The conjecture is so far, that the difference $F_z \propto N_{+1} - N_{-1}$ reduces this effect, which is why it does not affect the results in the spin degree of freedom as strongly. Nevertheless, an optimised preparation in the WG without sloshing has to be anticipated in future experiments to obtain cleaner results. Of course also further technical fluctuations can impact the result here.
Additionally, an in-depth study of the atom distributions and the macroscopic properties could shed light onto the behaviour of a vector soliton moving on an accelerating background.
However, a separation of the previously adjacent evaluation regions was introduced to account for classical correlations prevalent at the boundary. Nevertheless, the results remained in good agreement with the initially obtained ones and started to deviate after separations $d > 10.08\,\mu\mathrm{m}$. This is related to a prominent cutting into the peak structures, which discards increasingly more atoms also at late times.

Throughout this thesis the only fluctuation source of interest concerned the positional stability in vertical direction of our local rotation. Further technical noise sources can be investigated and attempted to be stabilised, such as polarisation drifts due to a thermal sensitivity of the pellicle or intensity and wavelength fluctuations of the local rotation laser.

Building on the results obtained in this thesis, various next steps can be taken. Starting in the soltion separation phase, extracting all three spin observables $F_{x,y,z}$ simultaneously would enable to analyse possible correlations between the spin variables or even spin squeezing. Revealing squeezing properties demands that the fluctuation reduction of one variable below the classical limit is at the cost of an increasing fluctuation in the conjugate variable. Further, the evolution of the internal spin state after the collision of two solitons can be studied, where correlations between spin observables were predicted in [16]. The preparation requires an additional control over the phase between the colliding solitons to ensure reproducible experiments, but also to allow to choose specific alignments, which have shown to impact the results before. Hence, a calibration of the magnetic field gradient is essential in order to prevent a deviating evolution of the phases. Aside from that, also more exotic configurations can be anticipated, like transferring components into the $F = 2$ manifold and analysing their propagation and collision with a soliton in $F = 1$. Such measurements could also help the development of a theoretical framework regarding this scenario, which to date is not clear yet.

Appendix A.

Fluctuations of a coherent state

A.1 Fluctuations of N^-

We consider the fluctuations of observables taking on the form

$$N^- = N_a - N_b, \tag{A.1}$$

where the subscript a and b are variables denoting two distinct modes we want to compare. They can represent the side-modes ± 1 as required in sec. 4.2.1 or different sides, e.g. left or right in sec. 5.2.2. Depending on the specific modes, we use that the total atom number is fixed by the sum of the respective atom numbers, so in this case $N = N_a + N_b$. This allows us to calculate the fluctuations in the difference A.1 for one case and conclude this result for all differences presented in fig. 5.3. So far no further assumptions are needed and the separation chosen to be arbitrary at this point. We can use the explicit representation of the variance in terms of the expectation values, i.e.

$$\begin{aligned} \Delta^2 N^- &= \langle (N^-)^2 \rangle - \langle N^- \rangle^2 \\ &= \langle (N_a - N_b)^2 \rangle - \langle N_a - N_b \rangle^2 \\ &= ... \\ &= \Delta^2 N_a + \Delta^2 N_b - 2(\langle N_a N_b \rangle - \langle N_a \rangle \langle N_b \rangle). \end{aligned} \tag{A.2}$$

We arrive at the last line by exploiting the linearity of the expectation value and rearranging the terms. The statistical nature is specified by the binomial distribution, where each atom is found with equal probability $p_a = p_b = 0.5$ either in a or b. This assumption is also justified by the idea that none of the two sides should be preferred by the atom if they are considered to be independent. The last term describes the covariance between the atom numbers on both sides and can be understood by noticing that each atom found on the left side, is missing on the right side. In that sense, the covariance term embodies the dependency between N^{l} and N^{r} and is defined for binomial distributed objects as

$$\begin{aligned} \mathrm{COV}(N_a, N_b) &= \langle N_a N_b \rangle - \langle N_a \rangle \langle N_b \rangle \\ &= -N p_a p_b. \end{aligned} \tag{A.3}$$

Additionally using that the variance of binomial distributed random variables is determined by

$$\Delta^2 N_{a,b} = N p_{a,b} (1 - p_{a,b}), \tag{A.4}$$

we can reformulate A.2 to

$$\begin{aligned} \Delta^2 N^- &= N p_a p_b + N p_a p_b + 2 N p_a p_b \\ &= N. \end{aligned} \tag{A.5}$$

After normalising the variance with the total atom number we achieve for equally distributed particles the limit

$$\Delta^2 \tilde{N}^- = 1 \tag{A.6}$$

A.2 Fluctuations of F_z based on the populations

Calculating the fluctuations of the F_z spin necessitates to consider $a = +1$ and $b = -1$ in eq. A.1. We further normalise this quantity with the average total atom number $\bar{N}$ and obtain

$$F_z = \frac{N_{+1} - N_{-1}}{\bar{N}}. \tag{A.7}$$

The variance of this quantity depends now on the variance of the imbalance between the side-modes

$$\Delta^2 F_z = \frac{\Delta^2 N^-}{\bar{N}^2}, \tag{A.8}$$

where the constant factor is pulled out squared. Since we aim to compare the fluctuation of any observable to the limit set by a coherent state, it is more meaningful to use the unnormalised $F_z = N^-$ and utilised solely $\bar{N}$ for normalisation as

$$\Delta^2 F_z = \frac{\Delta^2 N^-}{\bar{N}}. \tag{A.9}$$

In contrast to the difference between two sides, where we just sum up the atoms inside an evaluation region, we now have to consider now that the local rotations exerts spatially varying profiles according to the Rabi frequency $\Omega(x)$. To capture this we can use eq. A.5 to write

$$\begin{aligned} \Delta^2 N^- &= N p_{+1} p_{-1} + N p_{+1} p_{-1} + 2N p_{+1} p_{-1} \\ &= 4N p_{+1} p_{-1}, \end{aligned} \tag{A.10}$$

and calculate the probabilities inside this certain evaluation region relative to the total number $N = N_{+1} + N_0 + N_{-1}$.

$$p_{\pm 1} = \frac{N_{\pm 1}}{N} \tag{A.11}$$

A.3 Calibrating a $\pi/2$ rotation from $|1,0\rangle$

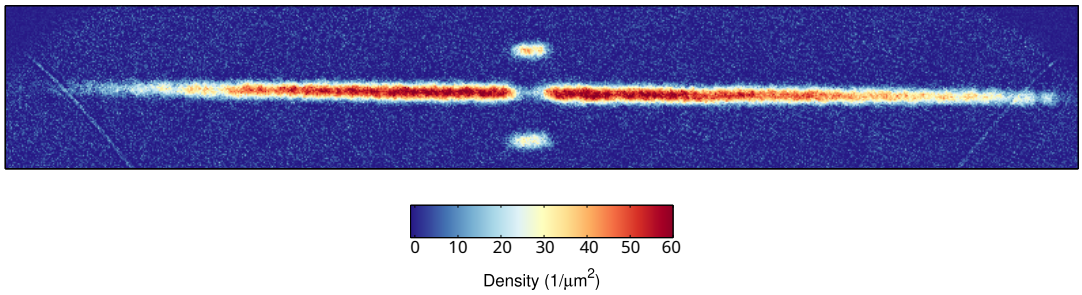

FIGURE A.1: The shot used for the calibration of a $\pi/2$ local spin rotation from $|1,0\rangle$. At 60 µs almost the entire population in the rotation region has been symmetrically transferred to the side-modes, as anticipated.

Appendix B.

Calculating the optimal reference pictures

As mentioned earlier, in order to be able to detect quantum effects, such as correlations or even entanglement, the necessity of sufficiently low noise, or more precisely fluctuations on coherent state level in the resulting data, is of major importance.

Before starting to analyse the measured data, we therefore process the raw data further to reduce the noise generated during the imaging process and remove fringe structures from the images. In the atom picture shown in fig. B.1, these fringes appear as diagonal stripes over the image. The general idea of this algorithm has been discussed before in [54].
When imaging the experiment, the CCD is written from top to bottom. We first image the atoms in the $F = 2$ manifold with its reference picture and repeat then the same for $F = 1$. The reference picture is just an empty picture of the specific manifold, without any atoms but with imaging light, to get an estimation of the imaging noise produced in this shot and identify fringes. The idea is now to use the reference pictures of the individual hyperfine-manifolds and calculate an optimal reference picture for each atom image in the respective manifold. This is done by an linear optimisation algorithm which effectively takes on the form

$$A \cdot X = B, \tag{B.1}$$

where A is the matrix containing the information about all reference pictures, B the vector containing the information about one specific picture where we imaged atoms and X the vector containing the weights that translate between these to matrices. For A and B, we slice the same part out of the reference picture, where we do not have any atoms imaged, and atom picture (see fig. B.1). These regions are called masks and determine the size of the matrices, since they contain the 1D projection of the pixel information. The other value necessary to determine the matrix A is the library size l, so the amount of reference pictures we actually use for the optimisation. The entire process of solving eq. B.1 is done for every single shot, allowing us to determine different sets of weights fulfilling the equation

$$r_{\mathrm{opt},n} = \sum_i x_{i,n} r_i \tag{B.2}$$

with the individual weight x_i and the respective reference picture r_i. In that manner we determine a new optimal reference picture $r_{\mathrm{opt},n}$ for the n-th image. Ultimately, we extract the data from each shot, considering its new optimal reference picture.
For large data sets, the time performance of solving B.1 depends on the provided processing power of the used computer, since the matrix A gets increasingly larger

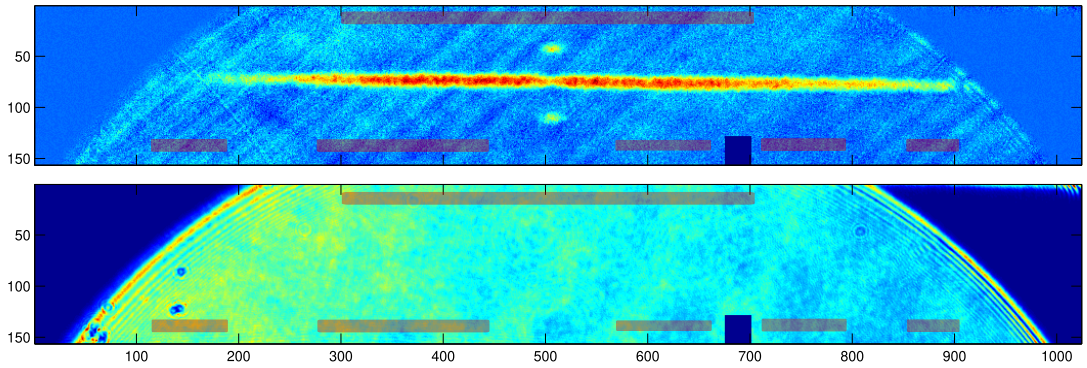

FIGURE B.1: Image taken of the $F = 1$ manifold for the readout of F_z with atoms and without atoms (reference picture). The information inside the red boxes (masks) is used for the optimal reference picture analysis. The regions are set equal for all images in $F = 1, 2$. The scale of both axis denote pixels.

with the number of shots taken in the experiment. A way to account for this, but at the same time ensure that the optimisation works sufficiently precise is to consider only a sub-set of reference pictures closest in time to the respective realisation. In that fashion, for the i-th shot, only the c reference pictures before and after are considered, the size of the reference picture library therefore reduced to $l = 2c + 1$ for all realisations instead of the entire n pictures. This step can be justified by the assumption that the experimental conditions undergo slight drifts over time resulting in a possibly not ideal comparability of two largely time-separated experimental realisations. The concept of a reduced reference library and the necessity to update it, to ensure the pictures closest in time are included, is presented in fig. B.2. The choice of the parameter c must assure a sufficiently large reference picture library, while at the same time keeping the calculation time reasonable. Since we do not have even earlier images at the beginning of the analysis, we have to consider only future images at this point. The idea is here to not fix the number of images before and after the current analysed shot c, but to fix the size of the reference library l. The further the number of analysed images proceeds, more previous reference pictures, relative to the currently analysed shot, are used. Additionally, after the number of analysed pictures surpasses $l/2$, the reference library gets updated for every further shot. The oldest reference picture is ejected while the next reference picture in time is included, until the library has been iterated to the end of all reference pictures. From this point on the library remains constant until the end of the analysis.

Throughout the analyses in this thesis we consider reference libraries containing 500-1100 pictures, depending on the measurement. Since we measure roughly 60 realisations per hour, we therefore consider the reference pictures in a time interval of $\sim 9 - 20$ hours.

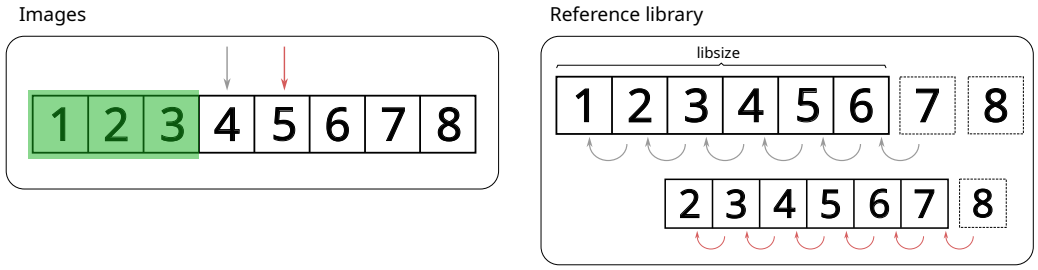

FIGURE B.2: Sketch of the refilling of the reference picture library, if the libsize is not including all reference pictures, i.e. libsize $l = 6 < N_{\text{images}} = 8$ in the example shown here. The i-th reference picture is taken together with the i-th image and carries its timestamp. For every image an optimal reference picture is calculated using the reference library. If the condition $N_{\text{analyzed}} > l/2$ is fulfilled, the reference library gets updated by including the next reference picture in time, while keeping the libsize constant. In the case here, the first update occurs for the analysis of the fourth image. For the update all entries in the reference library are shifted to the left, ejecting the first entry and including the new picture in the last slot. The reference library is now updated for every further image, until it is shifted to the end of accessible reference pictures, where it remains unchanged until the end of the image library is reached.

Bibliography

[1] Bose. "Plancks gesetz und lichtquantenhypothese". In: *Zeitschrift für Physik* 26.1 (1924), pp. 178–181.

[2] Albert Einstein. "Quantentheorie des einatomigen idealen gases. zweite abhandlung". In: *Albert Einstein: Akademie-Vorträge: Sitzungsberichte der Preußischen Akademie der Wissenschaften 1914–1932* (2005), pp. 245–257.

[3] Mike H Anderson et al. "Observation of Bose-Einstein condensation in a dilute atomic vapor". In: *science* 269.5221 (1995), pp. 198–201.

[4] Kendall B Davis et al. "Bose-Einstein condensation in a gas of sodium atoms". In: *Physical review letters* 75.22 (1995), p. 3969.

[5] Curtis Charles Bradley, CA Sackett, and RG Hulet. "Bose-Einstein condensation of lithium: Observation of limited condensate number". In: *Physical Review Letters* 78.6 (1997), p. 985.

[6] Giovanni Modugno et al. "Bose-Einstein condensation of potassium atoms by sympathetic cooling". In: *Science* 294.5545 (2001), pp. 1320–1322.

[7] Sebastian Kraft et al. "Bose-Einstein condensation of alkaline earth atoms: Ca 40". In: *Physical review letters* 103.13 (2009), p. 130401.

[8] Simon Stellmer et al. "Bose-Einstein condensation of strontium". In: *Physical review letters* 103.20 (2009), p. 200401.

[9] Mingwu Lu et al. "Strongly dipolar Bose-Einstein condensate of dysprosium". In: *Physical review letters* 107.19 (2011), p. 190401.

[10] Takeshi Fukuhara, Seiji Sugawa, and Yoshiro Takahashi. "Bose-Einstein condensation of an ytterbium isotope". In: *Physical Review A* 76.5 (2007), p. 051604.

[11] G Thalhammer et al. "Double species Bose-Einstein condensate with tunable interspecies interactions". In: *Physical review letters* 100.21 (2008), p. 210402.

[12] Martin W Zwierlein et al. "Observation of Bose-Einstein condensation of molecules". In: *Physical review letters* 91.25 (2003), p. 250401.

[13] David C Aveline et al. "Observation of Bose–Einstein condensates in an Earth-orbiting research lab". In: *Nature* 582.7811 (2020), pp. 193–197.

[14] Dan M Stamper-Kurn and Masahito Ueda. "Spinor Bose gases: Symmetries, magnetism, and quantum dynamics". In: *Reviews of Modern Physics* 85.3 (2013), p. 1191.

[15] Barbara Prinari, Federica Vitale, and Gino Biondini. "Dark-bright soliton solutions with nontrivial polarization interactions for the three-component defocusing nonlinear Schrödinger equation with nonzero boundary conditions". In: *Journal of Mathematical Physics* 56.7 (2015), p. 071505.

[16] Stefan Lannig. "Vector Solitons and Different Scenarios of Universal Dynamics in a Spin-1 Bose-Einstein Condensate". PhD thesis. Heidelberg University, 2022.

[17] Stefan Lannig et al. "Collisions of three-component vector solitons in Bose-Einstein condensates". In: *Physical Review Letters* 125.17 (2020), p. 170401.

[18] J Sakurai and J Napolitano. "Modern quantum mechanics. 2-nd edition". In: *Person New International edition* (2014).

[19] Claude Cohen-Tannoudji, Bernard Diu, and Frank Laloe. "Quantum Mechanics, Volume 1". In: *Quantum Mechanics* 1 (1986), p. 898.

[20] Lev Davidovich Landau and Evgenii Mikhailovich Lifshitz. *Quantum mechanics: non-relativistic theory*. Vol. 3. Elsevier, 2013.

[21] Philipp Kunkel. "Splitting a Bose-Einstein condensate enables EPR steering and simultaneous readout of noncommuting observables". PhD thesis. Heidelberg University, 2019.

[22] Lev Pitaevskii and Sandro Stringari. *Bose-Einstein condensation and superfluidity*. Vol. 164. Oxford University Press, 2016.

[23] Franco Dalfovo et al. "Theory of Bose-Einstein condensation in trapped gases". In: *Reviews of modern physics* 71.3 (1999), p. 463.

[24] Yuki Kawaguchi and Masahito Ueda. "Spinor bose–einstein condensates". In: *Physics Reports* 520.5 (2012), pp. 253–381.

[25] Lev P Pitaevskii. "Vortex lines in an imperfect Bose gas". In: *Sov. Phys. JETP* 13.2 (1961), pp. 451–454.

[26] Eugene P Gross. "Structure of a quantized vortex in boson systems". In: *Il Nuovo Cimento (1955-1965)* 20.3 (1961), pp. 454–477.

[27] Fabrice Gerbier et al. "Resonant control of spin dynamics in ultracold quantum gases by microwave dressing". In: *Physical Review A* 73.4 (2006), p. 041602.

[28] Shun Uchino. "Spinor Bose gas in an elongated trap". In: *Physical Review A* 91.3 (2015), p. 033605.

[29] Maxim Olshanii. "Atomic scattering in the presence of an external confinement and a gas of impenetrable bosons". In: *Physical review letters* 81.5 (1998), p. 938.

[30] Sergei V Manakov. "On the theory of two-dimensional stationary self-focusing of electromagnetic waves". In: *Soviet Physics-JETP* 38.2 (1974), pp. 248–253.

[31] PG Kevrekidis and DJ Frantzeskakis. "Solitons in coupled nonlinear Schrödinger models: a survey of recent developments". In: *Reviews in Physics* 1 (2016), pp. 140–153.

[32] John Scott Russell. *Report on Waves: Made to the Meetings of the British Association in 1842-43*. 1845.

[33] Akira Hasegawa. "An historical review of application of optical solitons for high speed communications". In: *Chaos: An Interdisciplinary Journal of Nonlinear Science* 10.3 (2000), pp. 475–485.

[34] Thomas Heimburg and Andrew D Jackson. "On soliton propagation in biomembranes and nerves". In: *Proceedings of the National Academy of Sciences* 102.28 (2005), pp. 9790–9795.

[35] Hidekazu Kuwayama and Shuji Ishida. "Biological soliton in multicellular movement". In: *Scientific reports* 3.1 (2013), p. 2272.

[36] Mark J Ablowitz, MA Ablowitz, and Peter A Clarkson. *Solitons, nonlinear evolution equations and inverse scattering*. Vol. 149. Cambridge university press, 1991.

[37] Aleksei Shabat and Vladimir Zakharov. "Exact theory of two-dimensional self-focusing and one-dimensional self-modulation of waves in nonlinear media". In: *Sov. Phys. JETP* 34.1 (1972), p. 62.

[38] Helmut Strobel. "Fisher Information and entanglement of non-Gaussian spin states". PhD thesis. Heidelberg University, 2015.

[39] Stefan Lannig. *Experimental Control of a Spin-1 Bose-EinsteincCondensate*. Master Thesis. 2018.

[40] Rudolf Grimm, Matthias Weidemüller, and Yurii B Ovchinnikov. "Optical dipole traps for neutral atoms". In: *Advances in atomic, molecular, and optical physics*. Vol. 42. Elsevier, 2000, pp. 95–170.

[41] Claude Cohen-Tannoudji, Jacques Dupont-Roc, and Gilbert Grynberg. *Atom-photon interactions: basic processes and applications*. John Wiley & Sons, 1998.

[42] Fam Le Kien, Philipp Schneeweiss, and Arno Rauschenbeutel. "Dynamical polarizability of atoms in arbitrary light fields: general theory and application to cesium". In: *The European Physical Journal D* 67 (2013), pp. 1–16.

[43] Nathan Goldman et al. "Light-induced gauge fields for ultracold atoms". In: *Reports on Progress in Physics* 77.12 (2014), p. 126401.

[44] Adam Fallon, Robert Leonard, and Charles Sackett. "High-precision measurements of the 87 Rb D-line tune-out wavelength". In: *APS Division of Atomic, Molecular and Optical Physics Meeting Abstracts*. Vol. 2016. 2016, N5–009.

[45] G Reinaudi et al. "Strong saturation absorption imaging of dense clouds of ultracold atoms". In: *Optics letters* 32.21 (2007), pp. 3143–3145.

[46] Wolfgang Muessel et al. "Optimized absorption imaging of mesoscopic atomic clouds". In: *Applied Physics B* 113 (2013), pp. 69–73.

[47] Jakob Steck. *Noise Characterization of Local Spin Rotations in a Spin-1 Bose-Einstein Condensate*. Bachelor's Thesis. 2021.

[48] IC Chang. "Acousto-optic devices and applications". In: *Handbook of optics* 2 (1995), pp. 12–1.

[49] Anika Frölian. *Implementation of local addressability in a Bose-Einstein Condensate*. Master Thesis. 2017.

[50] Catherine Forbes et al. *Statistical distributions*. John Wiley & Sons, 2011.

[51] Avery McIntosh. "The Jackknife estimation method". In: *arXiv preprint arXiv:1606.00497* (2016).

[52] Nir Bar-Gill et al. "Einstein-Podolsky-Rosen correlations of ultracold atomic gases". In: *Physical review letters* 106.12 (2011), p. 120404.

[53] Philipp Kunkel et al. "Spatially distributed multipartite entanglement enables EPR steering of atomic clouds". In: *Science* 360.6387 (2018), pp. 413–416.

[54] CF Ockeloen et al. "Detection of small atom numbers through image processing". In: *Physical Review A* 82.6 (2010), p. 061606.

Acknowledgements

It is the people around us that enable us to go through the hard times of a project like this and life in general. Many thanks go to the people who supported and helped me throughout the past year not just professionally but also morally to complete this thesis:

My first and foremost thanks go to Markus for taking me into his group and giving me the opportunity to work on this fascinating experiment. His approachable nature, enthusiasm and constant desire to push ideas and people further were truly inspiring to witness.

I thank Stefan for his supervision of this thesis over the past year. Without his insight on this topic, experimental questions and support on the technical implementation, this project would have been significantly harder to realise.
Equally I thank Helmut, who was never too busy to take his time for discussions on misunderstood concepts but also theoretical aspects. It was enlightening to learn from his intuition on physical processes and ability to solve experimental problems in the lab seemingly with ease.

My heartfelt thanks goes also to Christiane, who had the thankless task to run ever so often after me regarding any administrative question, but showed remarkable patience and kindness in doing so.

I sincerely thank Yannick and Lukas for their comments on my script. Their look from the outside helped to clarify this thesis and to finish it in a decent way.

Sometimes you find special friends in places you would have not expected. In that spirit, I thank Yannick and Alex for the past 1 1/2 years in the BEC-team. I will truly miss the time in the office and lab, consisting the entire spectrum of serious and not so serious talks, the banter and memorable evenings, but also scientific discussions and support throughout the process. I appreciated every minute with you guys and look forward to the future! And of course I cannot not mention the entire hallway on the second floor of the KIP, i.e. the SynQS. No matter if it was at lunch, in coffee breaks or during one of the many other events: The many funny discussions really eased the time and gave often enough a different perspective on things.

I am also grateful to have met Micha, Lukas and Felix during the first weeks at Uni. Whatever changed around us, however we evolved over time, we never lost sight of each other over the past years and accompanied us also through the harder times of being a student.

Special thanks go to the group of people - namely Andrej, Evita, Lea, Tobi, Frida, Laura, Joel, Steen, Maike, Ian - who made Heidelberg a home for me over the past years and, although now partially spread all over the world, have become more than just friends. Everybody should hope to find people who can lighten up even the darkest days.

And, I naturally want to deeply thank my parents, for making the life possible I have and the support they give me in every decision I make.

Declaration of Authorship

I, David Feiz Bakhsh Bazargani, declare that this thesis titled, “Noise reduction of local spin rotations and analysis of the three-component vector soliton formation” and the work presented in it are my own.

Signed:

Date: